INTRODUCTION

Plasmas are nowadays widely applied in the research domain and in industrial exploitation. Since plasma parameters are quantities that can be easily influenced by the measurement set-up, particular attention should be paid in the plasma experiment phase, during the development and application of the diagnostic techniques.

As regards the diagnostic techniques, two different classes can be distinguished: passive and active.

In the former case, the radiation from the plasma is studied. From the technical point of view it is a relatively simple application even if the phase of the result interpretation can be relatively complicated. In the latter case, an interaction with the plasma takes place. For example, a microwave beam can be directed to the plasma. This can offer much more information about the plasma itself, but is both more demanding on the experimental setup and can interfere with the object of study.

The main aim of this thesis was the development of different plasma diagnostic techniques, both active and passive. Those techniques were applied in different plasmas. Even if this work is split in two parts, each referring to a different experiment, the common basis still exists and has to be searched in the study and in the integration of those plasma measurements methods.

The first part of this work concerns a magneto hydrodynamic (MHD) power extraction experiment (Chapter 1), where electrical characterization was performed (Chapter 3 and 4). The more difficult task that had to be considered in this kind of plasma was the non-equilibrium technique used for ionization. In order to gain information on its parameters a, microwave measurement set-up was firstly studied (Chapter 2) and later realized (Chapter 4).

Plasma measurements with an active technique such as a microwave beam, allows. With a microwave measurement set-up it is possible to time resolve the electron number density by means of wave absorption and phase shifting. However this kind of technique has a lot of disadvantages: firstly the beam itself cannot be managed easily. A lot of equipment is necessary; for example a wave guide, emitting horns, a receiver, three stab tuners, crystal diodes and mixers. Besides this, if microwave power and frequency are not chosen carefully, the beam could affect the plasma with an energy deposition on it.

The second part of this thesis is still related to magneto hydrodynamics. The experiment described aims to demonstrate the feasibility to influence fluiddynamic parameters on a hypersonic flow by means of the MHD interaction (Chapter 5 and 8). At this stage, conjointly with electrical measurements and fast gating imaging (Chapter 9), a broad application of emission spectroscopy was chosen as a diagnostic technique (Chapter 10). Unfortunately, this type of hypersonic plasma had been proven to lie far beyond equilibrium, so several assumptions were necessary for the relative interpretation of the spectroscopic results (Chapter 6 and 7).

Emission spectroscopy can be used to measure the Atomic State Distribution Function (ASDF). In general, the occupation of excited levels depends on their energies, the electron density and the electron temperature. Therefore, from the ASDF the electron density and temperature can in principle be derived. This can work only in plasmas which are not too far from (Boltzmann and Saha) equilibrium. The need for assumptions on equilibrium departure is always a serious limitation in the measurement of electron density and temperature, if plasmas have a small scale and a low pressure as in the cases analyzed.

PART I

1. The MHD Power Extraction Experiment

1.1 Introduction

With increasing demands for high altitude, high velocity flight together with the associated flow control and power requirements, the theoretical applicability of MHD interaction becomes increasingly evident. Using efficient, non-equilibrium ionization methods, it has been shown that the amount of power that can be coupled out of such a flow can be significantly higher than the theoretical power requirements of ionization.[i,ii,iii] Magnetohydrodynamic (MHD) generators have been the focus of research for several decades. These devices have several attractive features in that no moving parts are involved in the process of power extraction, and their performance increases with the increasingly high velocity and rarified flow encountered in such cases as high altitude flight and reentry vehicles. In ground based generation, MHD generators have the potential advantage of using the direct exhaust from a combustion process as a working fluid. Because the exhaust is at a higher temperature than the steam which involve through turbines in conventional power plants, the potential entropy losses are lower. The first recorded attempt to develop an MHD generator was conducted at the Westinghouse Research Laboratories around the Second World War.[iv] Since then, many research organizations around the world have been involved in developing new approaches to design efficient generators.

The basic principle for MHD power extraction is simple. The generator produces power by passing a high-velocity, conducting fluid through a strong magnetic field. In most cases, ionized gas is used as a conducting fluid. Some other examples include liquid metal as a working fluid[v]. As the ionized gas passes through a magnetic field, an EMF is produced, resulting in a current that is drawn off to an external load. To achieve high power extraction and efficiency in an MHD generator, the conductivity of the working fluid is critical. This poses the single greatest challenge in gas flow MHD generators. Thermal ionization of most gasses, certainly those encountered in flight and standard combustion, is not significant below temperatures of around 4000 Kelvin. This places severe limitations on the range of materials that can be used in such a generator. Of particular concern is the electrode material which is necessarily in contact with the ionized flow. While it is possible to add seed materials to the flow to reduce the effective ionization potential, the requisite low ionization energy in such a material ensures that it will be highly reactive. Addition of alkali metals such as Cesium or Potassium can reduce necessary ionization temperatures to the range of 1800 to 3000 K. Sodium, Barium, and

Strontium have also been explored to this end.[vi] Technical problems involved in obtaining thermal ionization have been detailed by Muntenburch.[vii]

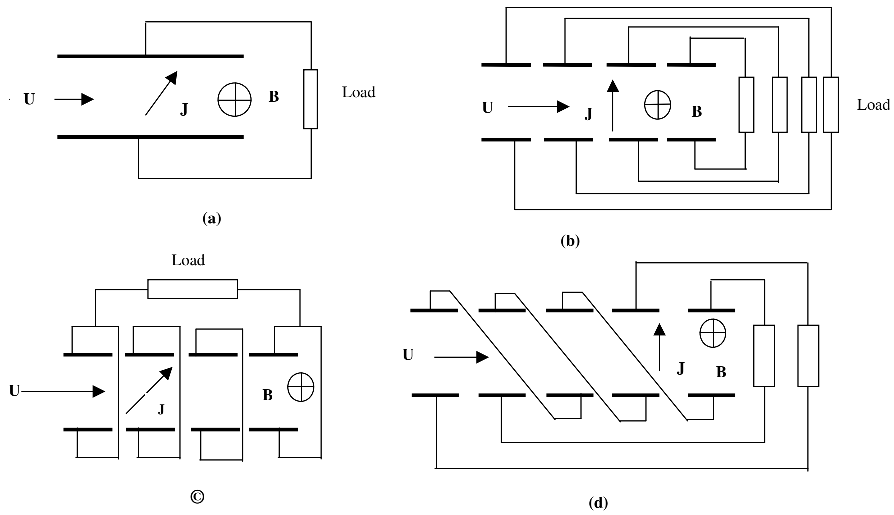

Fig. 1.1: Basic MHD Generator Configurations: a) Faraday Generator b) Faraday Segmented Generator c) Hall Generator d) Segmented Cross-linked Generator.

The collisionality of electrons in the flow has two principle effects: collisions decrease the conductivity of the flow, thereby hampering power extraction, but collisionality is also necessary to keep the charge carriers moving along with the flow. This latter condition is critical because, for nearly all MHD generators, the vast majority of the enthalpy of the flow is contained in the neutral species. This energy is transferred to the electrons via collisions and coupled out via Lorentz forces as the electrons travel through an applied magnetic field.

As it turns out, the collisionality, and its resultant effect on the conductivity of the flow, can have a complicated effect on the nature of the MHD interaction with the flow. The two most relevant parameters in assessing the effects of collisionality in an MHD generator are the electron Hall parameter (Ω_e) and the loading factor (k). The Hall parameter is defined as the ratio of the electron-cyclotron frequency (eB/m) to the electron collision frequency (ν_e). The load factor is defined as the ratio of the voltage across the generator to the theoretical EMF generated across the flow through the magnetic field. It should be pointed out that issues such as non-uniform flow and conductivities, cases where electrons are not the chief current carriers, and cases where the

magnetic field generated by the MHD current is large, will complicate the above arguments significantly.
Stated differently, the load factor may be viewed as the ratio of the current drawn to the maximum short circuit current. For high Hall parameters, the electrons tend to spiral around magnetic field lines rather than convect with the flow. This results in an upstream buildup of negative charge causing what is referred to as the Hall field. High Hall parameters also result in the conductivity becoming a tensor with relatively low conductivity across the magnetic field and higher conductivity along the magnetic field.
There are four main classes of MHD generators referred to as Hall and Faraday generators. These are diagrammed in figure 1.1**.** Faraday generators are ideal for low Hall parameters. Hall generators are suitable for high Hall parameters**.**

1.2 Ionization

MHD power extraction onboard a hypersonic vehicle can offer high levels of power generation for use by advanced payloads or engine bypass architectures[viii]. However, the requisite power necessary to maintain ionization (and conductivity) is of critical importance to any realistic vehicle. The power required to maintain a given electron number density is a function of two quantities: energy cost per electron, and rate of electron loss. There are several parameters of interest in hypersonic flow which scale favorably for MHD applications including:

Low density flow- increases conductivity for a given electron number density while also decreasing the power required to sustain a given electron number density by decreasing the rate of electron attachment.

High velocity flow- provides attractive scaling of MHD effects primarily by increasing the voltages associated with an MHD generator. Interestingly, because the flow time through an MHD channel is typically much greater than the lifetime of an ionized electron in the flow, the increased mass flow rate associated with increasing velocity will, in most cases, incur no penalty with regard to the power requirements necessary to maintain ionization (as opposed to seeding methods).

High temperature- associated with any hypersonic vehicle can often be used as a source of ionization – or to reduce the cost of ionization.

Because thermal ionization at the static temperatures in Mach < 12 flow is not possible without prohibitive levels of seeding (considering the high mass flow), non-equilibrium ionization methods must be employed. From a practical point of view, these non-equilibrium methods of ionization must be able to generate and sustain the ionization with the lowest power input. As stated previously, the power budget of sustaining a non-equilibrium plasma with a prescribed number density is proportional to the energy cost of creating a new electron in the plasma. When a non-equilibrium plasma is sustained by a DC or oscillating electric field, the electron energy balance is determined by the electron energy gain from the field and energy losses in various inelastic and elastic processes. Thus the electron temperature for a given set of gas parameters is defined by the ratio of electric field strength to the gas number density (E/N), or at low densities, by the ratio of electric field strength to the field oscillation frequency, E/ω.[ix] Typical values of E/N in non-equilibibrium discharges in molecular gases lie in the range $(1\text{-}6)\times10^{-16}$ V cm^2. The corresponding electron temperatures defined by the electron distribution function's (typically non-Maxwellian) slope at low energy are in the range 1-3 eV[ix]. Under these conditions, only a small fraction of the plasma electrons are capable of ionization requiring 10-15 eV energy. The vast majority of electron collisions result in electron energy loss, but produce no ionization. This energy loss is significant because high energy electrons are necessary to produce ionization. Therefore, only a very small fraction of the power (less than 0.1%) is actually spent on ionization, the corresponding energy cost being several tens of keV per electron[x].

In order to achieve high ionization efficiency, it would be desirable to have electrons of very high energy (hundreds of thousands of electron volts). In this regard, high energy electron beams are a natural choice. Injection of electrons accelerated to keV and higher energies into a gas results in ionization cascades as the beam propagates and loses its energy. The resulting energy cost per electron is around 34 eV for air, which is only a few times greater than the ionization energy of air molecules.[i,ii,iii] Models for analyzing the plasmas generated by high energy electron beams have already been applied to supersonic MHD power generation and flow controls.[x,xi,xii] Although electron beams are one of the most efficient way known of creating non-equilibrium plasmas, some inherent practical difficulties cannot be ignored. Problems related to mechanical and thermal strengths of injection foil are the main concern, and beam scattering in high-density gases can pose significant constraints on gas penetration.

Problems related to electron-beam based ionization have given way to alternative techniques for producing high-energy electrons. Plasma generation by high-voltage DC pulses has been recently explored[i]. It has been argued that high-energy electrons can be produced by applying a strong electric field which should be strong enough to sustain a steady plasma with a given electron number density, and at the same time must be able to generate electrical breakdown of the gas. To maintain a prescribed level of ionization, a strong electric field should be applied for only a short time. Well before the plasma completely decays the next pulse is applied to generate new electrons. In this way a desired average electron number density can be sustained by matching pulse duration with the rate of recombination or attachment. An important factor in assessing the performance of the repetitive-pulse approach is that the reduced energy cost due to the strong electric field in the pulse is offset somewhat by the need to produce more electrons in the pulse than the required average electron number density in the flow.

Modeling results clearly indicate that the increased electric field in a high intensity electrical pulse, will lead to formation of a large group of high-energy electrons in a high-voltage, nanosecond pulse: this would cause a dramatic increase in ionization.[i,x] Results also reveal that very short, high-voltage pulses at very high repetition rates could sustain a prescribed average ionization level in air with the required power input significantly lower than that in a DC discharge.

In experimental work object of this thesis, a source of multi-kilovolt (2 ns, 100 kHz,~ 30 KV), nanosecond pulses with high repetition rate was used to ionize the flow through a Mach 3, continuous electrode Faraday MHD channel. Current/voltage characteristics of the channel are presented. Microwave absorption technique was fully developed and tuned on a static cell, as it produces a plasma with the same characteristics of the flowing experiment. Details on the experimental hardware, theory, and results have been included in chapter following.

1.3 Microwave as a Diagnostic System

For plasma with such a low degree of ionization, it was necessary to develop a suitable diagnostic system for a better comprehension of the phenomena involved in the discharge.

Microwave and infra-red diagnostic techniques that measure electron number density and collision frequency are essential for characterization of the phenomenon. For small scale, cold plasmas however, to observe a measurable effect, standard phase shift and transmission methods require a diagnostic frequency close to the plasma frequency. This result in a refractive index far from unity, which, in turn, causes significant reflection at the boundaries along with refraction, diffraction, and other three dimensional effects that are difficult to quantify or compensate for. It was developed a simple, non-intrusive microwave transmission diagnostic method applicable to small-scale plasmas and capable of measuring both electron number density and collision frequency was developed. To accomplish this, a magnetic field is applied across the plasma. By varying the intensity of the applied magnetic field, the frequency of the upper hybrid resonance for transmission of extraordinary waves, as predicted by the Asher-Appleton-Hartree dispersion relation, is scanned through the microwave diagnostic frequency. Qualitatively, the location of the absorption band depends on the electron number density, and the width of the band depends on the collision frequency. Because there is essentially zero transmission through the absorption band, the measurement relies on determination of the microwave frequency and the magnetic field intensity corresponding to zero transmission. This method has a considerable advantage over traditional microwave transmission methods, in which reflections at the edges of the plasma along with refraction, diffraction and impedance matching among the microwave antennas and the plasma can have a strong impact on the measurement[xiii].

2. Microwave Propagation Theory

2.1 Microwave Propagation

For a better comprehension about how microwaves can be usefully utilized in plasmas, it is necessary to give a better insight to their nature.

As with all electromagnetic waves, microwaves can be described by electric and magnetic fields, **E** and **H**, which are functions of space and time. The electric and magnetic fluxes, **D** and **B**, at any point are related to the field intensities by

$$\mathbf{D} = \varepsilon \mathbf{E} \tag{2.1}$$

$$\mathbf{B} = \mu \mathbf{H} \tag{2.2}$$

The electric permittivity, ε, and the magnetic permeability, μ, are scalar numbers in isotropic materials. These vector fields are all related by Maxwell's equations:

$$\nabla \cdot \mathbf{D} = \rho \tag{2.3}$$

$$\nabla \cdot \mathbf{B} = 0 \tag{2.4}$$

$$\nabla \times \mathbf{H} = \mathbf{i} + \frac{\partial \mathbf{D}}{\partial t} \tag{2.5}$$

$$\nabla \times \mathbf{E} = -\frac{\partial \mathbf{B}}{\partial t} \tag{2.6}$$

In a dielectric material, for which no free charges or currents exist, $\rho = 0$ and i = 0. Maxwell's equations may be rearranged by taking the curl of both sides of equation (2.6):

$$\nabla \times \nabla \times \mathbf{E} = -\nabla \times \frac{\partial \mathbf{B}}{\partial t} \,. \tag{2.7}$$

Using the vector relation $\nabla \times \nabla \times \mathbf{A} = \nabla(\nabla \cdot \mathbf{A}) - \nabla^2 \mathbf{A}$, this becomes

$$\nabla\left(\nabla \cdot \mathbf{E}\right) - \nabla^2 \mathbf{E} = -\nabla \times \frac{\partial \mathbf{B}}{\partial t}$$

$$\frac{1}{\varepsilon} \nabla\left(\nabla \cdot \mathbf{D}\right) - \nabla^2 \mathbf{E} = -\mu \frac{\partial}{\partial t}\left[\nabla \times \mathbf{H}\right]$$

$$-\nabla^2\mathbf{E} = -\mu\frac{\partial}{\partial t}\left[\frac{\partial\mathbf{D}}{\partial t}\right]$$

$$\nabla^2\mathbf{E} = \mu\varepsilon\frac{\partial^2\mathbf{E}}{\partial t^2}$$

$$\nabla^2\mathbf{E} - \mu\varepsilon\frac{\partial^2\mathbf{E}}{\partial t^2} = 0 \tag{2.8}$$

Under the same assumptions it may be shown in a from equation 2.5 that

$$\nabla^2\mathbf{H} - \mu\varepsilon\frac{\partial^2\mathbf{H}}{\partial t^2} = 0. \tag{2.9}$$

Equations 2.8 and 2.9 are wave equations with general solutions of the form

$$\mathrm{f}\left(\omega t + k_x x\right)\mathrm{g}\left(\omega t + k_y y\right)\mathrm{h}\left(\omega t + k_z z\right)\left(k_x\hat{\mathbf{i}} + k_y\hat{\mathbf{j}} + k_z\hat{\mathbf{k}}\right), \tag{2.10}$$

where $k_x^2 + k_y^2 + k_z^2 = k^2 = \omega^2\mu\varepsilon$ and the functional dependencies f, g, and h are determined by imposed boundary conditions. Any function may be treated as the sum of its fourier components, so that without loss of generality all solutions may be considered to be of the form

$$\begin{aligned} &A\cos\left(\omega t + k_x x + \phi_x\right)\cos\left(\omega t + k_y y + \phi_y\right)\cdot \\ &\cdot\cos\left(\omega t + k_z z + \phi_z\right)\left(k_x\hat{\mathbf{i}} + k_y\hat{\mathbf{j}} + k_z\hat{\mathbf{k}}\right) \end{aligned} \tag{2.11}$$

$$\text{or} \quad e^{j(\omega t \pm kz)} \tag{2.12}$$

The most basic microwave circuit element is the transmission line, or waveguide. The microwave field is contained within conducting waveguide walls, and in the ideal case is propagated without reflection or loss. This ideal case is achieved for a waveguide of uniform cross section in the limit of infinitely conductive walls. The wave equations are solved by applying boundary conditions for the electric and magnetic fields along the perimeter of the wall. These boundary conditions are best described by first considering Maxwell s' equations in their integral form:

$$\oint\!\!\oint_A \mathbf{D}\cdot d\mathbf{s} = q \tag{2.13}$$

$$\oint_A \mathbf{B} \cdot d\mathbf{s} = 0 \tag{2.14}$$

$$\oint_C \mathbf{H} \cdot d\mathbf{l} = \int_A \mathbf{i} \cdot d\mathbf{S} + \frac{\partial}{\partial t} \int_A \mathbf{D} \cdot d\mathbf{S} \tag{2.15}$$

$$\oint_C \mathbf{E} \cdot d\mathbf{l} = -\frac{\partial}{\partial t} \int_A \mathbf{B} \cdot d\mathbf{S} \tag{2.16}$$

These equations are equivalent to the differential form given by equations 2.3 to 2.6.

At the surface of an infinitely conductive waveguide wall, the tangential component of electric field, $\mathbf{E_t}$, must equal zero. This can be illustrated by considering a small rectangle enclosing a segment of the surface.

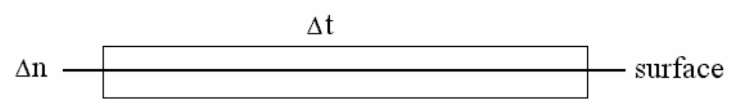

Fig. 2.1: Rectangular enclosure around the surface.

As the length *Δn* approaches zero, the area enclosed by the rectangle also approaches zero. In the limit of zero area, the integral $\int_A \mathbf{B} \cdot d\mathbf{S}$ equals zero, and so by equation (2.15) the line integral $\oint_C \mathbf{E} \cdot d\mathbf{l}$ must also equal zero. This line integral can be written as the sum of the integrals along the normal and tangential sides:

$$\begin{aligned} \oint_C \mathbf{E} \cdot d\mathbf{l} &= \int_n^{n+\Delta n} \mathbf{E_n}(t,n)\,dn + \\ &+ \int_t^{t+\Delta t} \mathbf{E_t}(t, n+\Delta n)\,dt + \int_{n+\Delta n}^{n} \mathbf{E_n}(t+\Delta t, n)\,dn + \int_{t+\Delta t}^{t} \mathbf{E_t}(t,n)\,dt \end{aligned}.$$

As the length *Δn* approaches zero, the integral of $\int \mathbf{E_n}\,dn$ must also approach zero. Thus the total contribution to the integral around the rectangle depends only on $\mathbf{E_t}$. The tangential electric fields on each side of the surface, $\mathbf{E_t}(t,n)$ and $\mathbf{E_t}(t,n+\Delta n)$, must therefore be equal. Because the wall is assumed to be infinitely conductive, $\mathbf{E_t}$ must be zero as an infinitely conductive surface will not support a tangential electric field.

The second boundary condition, $\frac{\partial \mathbf{B_n}}{\partial n} = 0$ at the wall, is proved using a volume element enclosing a portion of the surface.

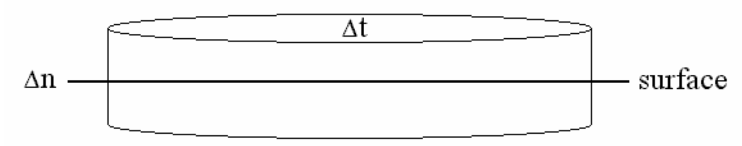

Fig. 2.2: Volume element enclosing the surface.

Applying the divergence theorem to equation 2.14 yields

$$\oiint_A \mathbf{B} \cdot d\mathbf{S} = 0 . \tag{2.17}$$

As the length Δn approaches zero, the contribution to this integral from the sides vanishes, so the magnetic field normal to the upper and lower surfaces, $\mathbf{B_n}(t,n+\Delta n)$ and $\mathbf{B_n}(t,n)$, must be equal. As was shown earlier, the tangential electric field is zero at the surface, so by equation 2.6 there can be no time dependent component of $\mathbf{B_n}$. If there is no initial magnetic field, $\mathbf{B_n}$ and $\mathbf{H_n}$ must remain zero at all later times.

The electric and magnetic fields inside the waveguide are more conveniently expressed in terms of their transverse and axial components. If the coordinates are chosen such that the axis of the waveguide lies in the z direction, the fields may be written as

$$\mathbf{E} = \mathbf{E_t} + \mathbf{E_z} \tag{2.18}$$

$$\mathbf{H} = \mathbf{H_t} + \mathbf{H_z} \tag{2.19}$$

The electric and magnetic fields in a waveguide are found by solving the wave equation and then applying the appropriate boundary conditions. A solution need only be found at one frequency, since any arbitrary solution may be formed from a linear combination of solutions at single frequencies. Also, the equations may be simplified by choosing the coordinate axes such that the propagation vector lies along the z axis. This will generate solutions of the form

$$\mathbf{E} = \left(\mathbf{e_t} + \mathbf{e_z}\right) e^{j(\omega t - \beta z)} \tag{2.20}$$

$$\mathbf{H} = \left(\mathbf{h_t} + \mathbf{h_z}\right) e^{j(\omega t - \beta z)} \tag{2.21}$$

where **e** and **h** are functions of x and y only, and β is a propagation constant. Substituting this form for the fields into Maxwell s' equations yields the reduced form

$$\nabla_{\mathbf{t}} \times \mathbf{e_t} = -j\omega\mu\mathbf{h_z} \tag{2.22}$$

$$\nabla_{\mathbf{t}} \times \mathbf{e_z} - j\beta\hat{\mathbf{k}} \times \mathbf{e_t} = -\hat{\mathbf{k}} \times \nabla_{\mathrm{t}}\, \mathrm{e_z} - j\beta\hat{\mathbf{k}} \times \mathbf{e_z} = -j\omega\mu\mathbf{h_t} \tag{2.23}$$

$$\nabla_{\mathbf{t}} \times \mathbf{h_t} = j\omega\varepsilon\mathbf{e_z} \tag{2.24}$$

$$\hat{\mathbf{k}} \times \nabla_{\mathrm{t}}\, \mathrm{h_z} + j\beta\hat{\mathbf{k}} \times \mathbf{h_t} = -j\omega\varepsilon\mathbf{e_t} \tag{2.25}$$

$$\nabla_{\mathbf{t}} \cdot \mathbf{h_t} = j\beta\mathbf{h_z} \tag{2.36}$$

$$\nabla_{\mathbf{t}} \cdot \mathbf{e_t} = j\beta\mathbf{e_z}\,. \tag{2.37}$$

Equations 2.5 and 2.6 have been split into axial and transverse components, resulting in six equations. Solutions may be decomposed into three separate cases: transverse electric, referred to as TE or H modes, for which $\mathbf{e_z} = 0$, $\mathbf{h_z} \neq 0$; transverse magnetic, referred to as TM or E modes, for which $\mathbf{h_z} = 0$, $\mathbf{e_z} \neq 0$; and transverse electromagnetic, or TEM waves, for which $\mathbf{e_z} = \mathbf{h_z} = 0$. The transverse electric case is considered first.

Splitting equation 2.9 into transverse and axial components, it is clear that both $\mathbf{H_t}$ and $\mathbf{H_z}$ must satisfy the wave equation separately. A solution for $\mathbf{H_z}$ will be found first. It will then be possible to determine the full field solution in terms of $\mathbf{H_z}$. Dividing the wave equation for $\mathbf{H_z}$ by the exponential term $e^{j(\omega t-\beta z)}$ and dotting with the unit vector in the z direction yields the following scalar equation for $\mathrm{h_z}$:

$$\nabla_{\mathrm{t}}^2\, \mathrm{h_z} + k_c^2\, \mathrm{h_z} = 0 \tag{2.28}$$

where the substitution $k_c^2 = k^2 - \beta^2$ has been made. By separation of variables,

$$\mathrm{h_z} = \left(A\cos k_x x + B\sin k_x x\right) * \left(C\cos k_y y + D\sin k_y y\right). \tag{2.29}$$

The boundary conditions are determined by the geometry of the waveguide. For a hollow rectangular guide of the type used in the experiments, let the interior dimensions be $\mathrm{a}\times\mathrm{b}$.

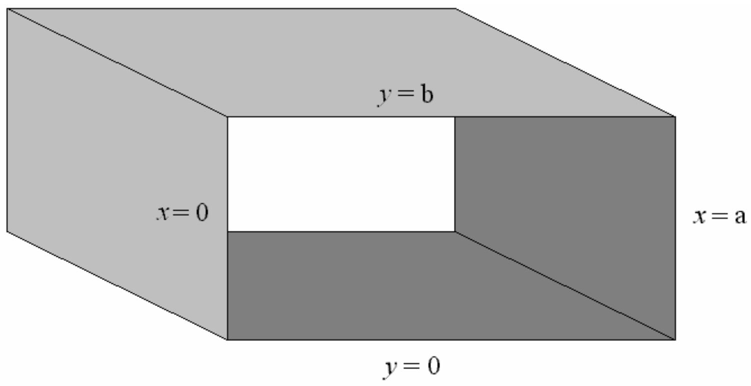

Fig. 2.3: Hollow rectangular waveguide.

Setting e_z and the tangential electric field to zero at the boundaries, the magnetic boundary conditions are found from equations 2.23 and 2.25 as

$$\frac{\partial \mathrm{h}_z}{\partial x} = 0 \ @ \ x = 0, a \tag{2.30}$$

$$\frac{\partial \mathrm{h}_z}{\partial y} = 0 \ @ \ y = 0, b \tag{2.31}$$

Applying these conditions to equation 2.29,

$$\mathrm{h}_z = A_{nm} \cos\left(\frac{n\pi x}{a}\right)\cos\left(\frac{m\pi y}{b}\right) \tag{2.32}$$

for integer values of n and m. The new coefficients for x and y are the eigenvalues of the propagation constants k_x and k_y. The remaining magnetic field components and the electric field components are found by substitution of this result into equations 2.22 to 2.27. A solution with particular values for n and m is referred to as the TE_{nm} mode.

Solutions to TM modes are found similarly from the wave equation for the axial electric field, analogous to equation 2.28:

$$\nabla_t^2 \mathrm{e}_z + k_c^2 \mathrm{e}_z = 0 \ . \tag{2.33}$$

The boundary condition that the tangential component of electric field must go to zero at the wall is imposed:

$$e_z = 0 \,@\, x = 0, a, \; y = 0, b \,, \tag{2.34}$$

which leads to a solution of the form

$$\mathrm{e}_z = A_{nm} \sin\left(\frac{n\pi x}{a}\right) \sin\left(\frac{m\pi y}{b}\right). \tag{2.35}$$

The remaining electric field components and the magnetic field components arefound from equations 2.22 through 2.27 using this result for e_z.

Note that in the solutions to the TE and TM waves, each mode corresponds to a different eigenvalue, k_c, determined by the relationship

$$k_{c,nm}^2 = \left(\frac{n\pi}{a}\right)^2 + \left(\frac{m\pi}{b}\right)^2. \tag{2.36}$$

Recall that the constant k_c is defined by $k_c^2 = \left(k^2 - \beta^2\right)$. Using the above relation for k_c and the definition $k = \sqrt{\omega^2 \mu\varepsilon} = \frac{2\pi}{\lambda}$ allows the propagation constant to be determined as

$$\gamma \equiv j\beta = j\sqrt{k^2 - k_c^2} = j\sqrt{\left(\frac{2\pi}{\lambda}\right)^2 - \left(\frac{n\pi}{a}\right)^2 - \left(\frac{m\pi}{b}\right)^2}\,. \tag{2.37}$$

This quantity can be either real or imaginary, depending on the sign of the quantity $k^2 - k_c^2$. The cutoff wavelength, where γ is equal to zero, is given by

$$\lambda_c = \frac{2\pi}{\sqrt{\left(\frac{n\pi}{a}\right)^2 + \left(\frac{m\pi}{b}\right)^2}} = \frac{2ab}{\sqrt{n^2 b^2 + m^2 a^2}}\,. \tag{2.38}$$

At wavelengths less than λ_c, γ is imaginary and microwaves propagate with a sinusoidal variation in the z direction of $e^{-\gamma z}$. However, at wavelengths greater than λ_c, γ is real and the factor $e^{-\gamma z}$ corresponds to an exponentially decaying wave. This is what is meant by cutoff. Tables 2.1a and 2.1b on the following pages list the transverse variation in electric and magnetic field components for TM and TE modes. The full field components are obtained by multiplying by the factor $e^{j(\omega t-\beta z)}$. Also given in the tables is the impedance Z_{nm} of each mode. From the relationship $k_0 > k_c$ for propagating waves, the impedance of TM modes can be seen to be less than the free space impedance Z_0, and the impedance of TE modes to be greater than Z_0.

Table 2.1a: Electric and magnetic field components of TM modes.

	TM modes
h_z	0
h_x	$\dfrac{E_{0,nm}}{Z_0}\dfrac{jk_0 m\pi}{b\left[\left(\frac{n\pi}{a}\right)^2+\left(\frac{m\pi}{b}\right)^2\right]}\sin\left(\frac{n\pi x}{a}\right)\cos\left(\frac{m\pi y}{b}\right)$
h_y	$-\dfrac{E_{0,nm}}{Z_0}\dfrac{jk_0 n\pi}{a\left[\left(\frac{n\pi}{a}\right)^2+\left(\frac{m\pi}{b}\right)^2\right]}\cos\left(\frac{n\pi x}{a}\right)\sin\left(\frac{m\pi y}{b}\right)$
e_z	$E_{0,nm}\sin\left(\frac{n\pi x}{a}\right)\sin\left(\frac{m\pi y}{b}\right)$
e_x	$-E_{0,nm}\dfrac{j\beta_{nm} n\pi}{a\left[\left(\frac{n\pi}{a}\right)^2+\left(\frac{m\pi}{b}\right)^2\right]}\cos\left(\frac{n\pi x}{a}\right)\sin\left(\frac{m\pi y}{b}\right)$
e_y	$-E_{0,nm}\dfrac{j\beta_{nm} m\pi}{b\left[\left(\frac{n\pi}{a}\right)^2+\left(\frac{m\pi}{b}\right)^2\right]}\sin\left(\frac{n\pi x}{a}\right)\cos\left(\frac{m\pi y}{b}\right)$

Z_{nm}	$Z_0 \dfrac{\beta_{nm}}{k_0}$

Table 2.1b: Electric and magnetic field components of TE modes.

	TE modes
h_z	$\dfrac{E_{0,nm}}{Z_0}\cos\left(\dfrac{n\pi x}{a}\right)\cos\left(\dfrac{m\pi y}{b}\right)$
h_x	$\dfrac{E_{0,nm}}{Z_0}\dfrac{j\beta_{nm}n\pi}{a\left[\left(\dfrac{n\pi}{a}\right)^2+\left(\dfrac{m\pi}{b}\right)^2\right]}\sin\left(\dfrac{n\pi x}{a}\right)\cos\left(\dfrac{m\pi y}{b}\right)$
h_y	$\dfrac{E_{0,nm}}{Z_0}\dfrac{j\beta_{nm}m\pi}{b\left[\left(\dfrac{n\pi}{a}\right)^2+\left(\dfrac{m\pi}{b}\right)^2\right]}\cos\left(\dfrac{n\pi x}{a}\right)\sin\left(\dfrac{m\pi y}{b}\right)$
e_z	0
e_x	$E_{0,nm}\dfrac{jk_0m\pi}{b\left[\left(\dfrac{n\pi}{a}\right)^2+\left(\dfrac{m\pi}{b}\right)^2\right]}\cos\left(\dfrac{n\pi x}{a}\right)\sin\left(\dfrac{m\pi y}{b}\right)$
e_y	$-E_{0,nm}\dfrac{jk_0n\pi}{a\left[\left(\dfrac{n\pi}{a}\right)^2+\left(\dfrac{m\pi}{b}\right)^2\right]}\sin\left(\dfrac{n\pi x}{a}\right)\cos\left(\dfrac{m\pi y}{b}\right)$

Z_{nm}	$Z_0 \dfrac{k_0}{\beta_{nm}}$

Because the propagation constants are different for each mode, some modes may be propagating while others are not. A standard rectangular waveguide typically has one dimension twice the length of the other, a = 2b. For this type of waveguide, the cutoff wavelengths for the first three modes are listed in Table 2.2 below.

Table 2.2: Cutoff wavelengths for cavity modes.

nm	λ_c
10	2a
01	a
11	$2a/\sqrt{5}$

Comparing equations 2.35 and 2.32 for TE and TM modes, it can be seen that the lowest order TM mode is the TM_{11} mode, since the trivial solution is obtained by setting n and m to zero. However, nontrivial TE modes exist for either n or m equal to zero. Between wavelengths of a and 2a only the TE_{10} mode propagates and all other modes are cut off. For this reason, the TE_{10} mode is known as the dominant mode, and it is in this single mode condition that microwave waveguides are typically operated.

The TE_{10} mode is sketched in figures 2.4a and 2.4b, showing the electric and magnetic field lines. Physically, the mode number for TE modes corresponds to the number of half wave oscillations of the electric field in the perpendicular and parallel directions, respectively. So for a TE_{10} mode, the electric field has a one half period sinusoidal oscillation perpendicular to the polarization vector, and is constant in the parallel direction. The waveguide sketches depicted in figures 2.4a and 2.4b below, are oriented such that the propagation vector is in the horizontal direction.

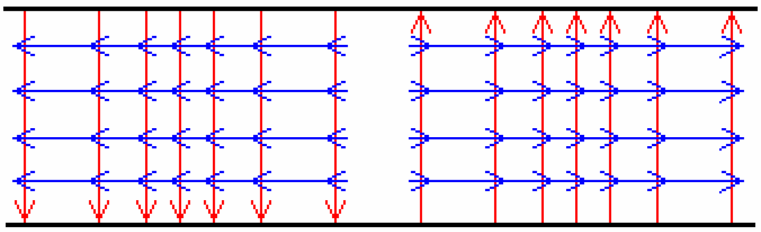

Fig 2.4a: E-plane field lines (electric field in red, magnetic field in blue).

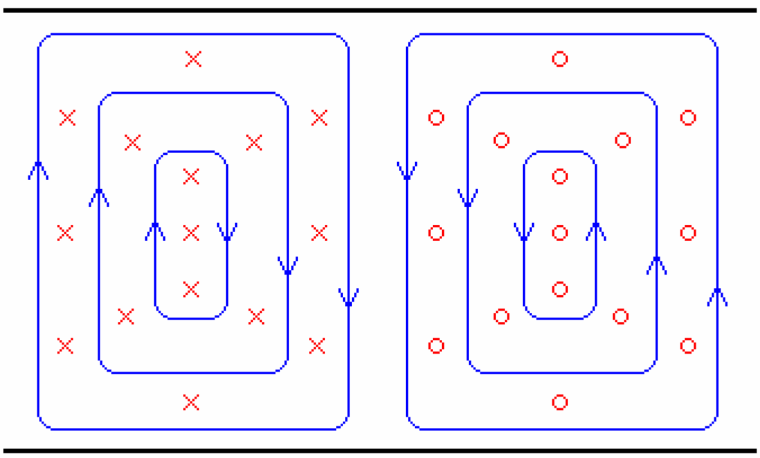

Fig 2.4b: H-plane field lines (electric field in red, magnetic field in blue).

A brief discussion of the third class of propagating wave solutions, the transverse electromagnetic wave, is in order. Following the form of equations 2.22 through 2.27 and setting the axial components of the electric and magnetic fields equal to zero. The Maxwell's equations may be written as

$$\nabla_t \times \mathbf{e}_t = 0 \tag{2.39}$$

$$\beta \hat{\mathbf{k}} \times \mathbf{e}_t = \omega \mu \mathbf{h}_t \tag{2.40}$$

$$\nabla_t \times \mathbf{h}_t = 0 \tag{2.41}$$

$$\beta \hat{\mathbf{k}} \times \mathbf{h}_t = -\omega \varepsilon \mathbf{e}_t \tag{2.42}$$

$$\nabla_t \cdot \mathbf{h}_t = 0 \tag{2.43}$$

$$\nabla_t \cdot \mathbf{e}_t = 0\,. \tag{2.44}$$

Equation 2.39 shows that **e** must be the gradient of a scalar potential function. In order for equation 2.44 to also be satisfied, the scalar function must be a solution to Laplace's equation:

$$\nabla_{\mathbf{t}}^{2}\Phi = 0\,. \tag{2.45}$$

The boundary condition $\mathbf{E_t} = 0$ implies that the gradient of Φ in the tangential direction, $\frac{\partial \Phi}{\partial s}$, must be zero along the boundary. The unique solution to Laplace's equation is then Φ equal to a constant. Physically, this is a statement that the voltage is uniform along the boundary, which clearly must be true for the infinitely conductive walls assumed in the problem. In this case $\mathbf{E} = \nabla\Phi = 0$ everywhere inside the perimeter of the waveguide, and the only solution is the trivial one. Therefore, TEM modes cannot be sustained by hollow conducting waveguides.

In a rectangular waveguide the propagation constant may be determined from equation 2.37, and is seen to depend upon the waveguide dimensions. A guide wavelength may be defined as

$$\lambda_g \equiv \frac{2\pi}{\beta} = \frac{2\pi}{\sqrt{\left(\frac{2\pi}{\lambda}\right)^2 - \left(\frac{n\pi}{a}\right)^2 - \left(\frac{m\pi}{b}\right)^2}}\,. \tag{2.46}$$

In the case of a single propagating TE_{10} mode, this expression becomes

$$\lambda_g = \frac{2\pi}{\sqrt{\left(\frac{2\pi}{\lambda}\right)^2 - \left(\frac{\pi}{a}\right)^2}} \tag{2.47}$$

and depends only on the larger dimension, a, of the rectangular guide. The guide wavelength is always greater than the free space wavelength, λ. It may vary between λ as $a \to \infty$, and infinity at $a = \frac{\lambda}{2}$. A guide which has a varying cross section along its length will allow propagation with a similarly varying guide wavelength. If the guide should become smaller than the cutoff dimension, corresponding to $a < \frac{\lambda}{2}$, then the wave will cease to propagate and instead will decay exponentially as an evanescent wave over a characteristic length scale $\frac{1}{\gamma}$, where

$$\gamma = \sqrt{\left(\frac{\pi}{a}\right)^2 - \left(\frac{2\pi}{\lambda}\right)^2} \,. \qquad (2.48)$$

As shown on Tables 2.1a and 2.1b, the wave impedance is also a function of both the mode number and the guide dimensions.

2.2 Microwave Behavior in Plasmas

The preceding section describes microwave propagation through a linear medium, for which μ and ε are constant. The free charges present in a plasma give rise to dispersion and attenuation.

Consider the displacement of electrons by an amount ξ due to an applied electric field $E = E_0 e^{j\omega t}$. The electrons will be accelerated by this field as

$$m\frac{d^2\xi}{dt^2} = -eE_0 e^{j\omega t} \qquad (2.49)$$

which, solving for ξ, becomes

$$\xi = \frac{e}{m\omega^2} E_0 e^{j\omega t} = \frac{e}{m\omega^2} E \qquad (2.50)$$

The current resulting from this electron motion will be

$$i = -ne\frac{d\delta}{dt} = -j\frac{ne^2}{m\omega} E \,. \qquad (2.51)$$

This expression can be rewritten in terms of a conductivity, σ, equal to $-j\frac{ne^2}{m\omega^2}$. This conductivity may also be expressed as a complex permittivity. Rewriting equation 2.5 in terms of the conductivity yields

$$\nabla \times \mathbf{H} = \left(\sigma + j\omega\varepsilon_0\right)\mathbf{E} \,. \qquad (2.52)$$

The two terms on the right hand side may be combined in a complex permittivity as

$$\varepsilon = \varepsilon_0 - j\frac{\sigma}{\omega}. \tag{2.53}$$

Using this definition, the propagation constant is

$$\beta = \sqrt{\frac{\varepsilon}{\varepsilon_0}}\frac{\omega}{c} = \sqrt{1-\frac{ne^2}{\varepsilon_0 m\omega^2}}\frac{\omega}{c}, \tag{2.54}$$

where the quantity $\sqrt{\frac{ne^2}{\varepsilon_0 m}}$ is the plasma frequency, ω_p. Equation 2.54 can be expressed in terms of this frequency as

$$\beta = \sqrt{1-\frac{\omega_p^2}{\omega^2}}\frac{\omega}{c}. \tag{2.55}$$

Note that this propagation constant is real only if the frequency of the incident wave is greater than the plasma frequency, and pure imaginary when the incident wave is at a lower frequency.

The preceding analysis neglects the effects of collisions. To first order, an average collision removes the directed velocity of an electron. This can be accounted for by adding another term to equation 2.49:

$$m\frac{d^2\delta}{dt^2} = -eE_0e^{j\omega t} - \nu m\frac{d\delta}{dt}, \tag{2.56}$$

where ν represents the collision frequency. The solution for δ then becomes

$$\delta = \frac{e}{m\omega(\omega - j\nu)}E_0e^{j\omega t}. \tag{2.57}$$

Substituting this result into equation 2.51 yields the current

$$i = \frac{-ne^2 j\omega}{m\omega(\omega - j\nu)}E_0e^{j\omega t} = \frac{-jne^2}{m(\omega - j\nu)}E_0e^{j\omega t} \tag{2.58}$$

and the conductivity

$$\sigma = \frac{-jne^2}{m(\omega - j\nu)} = \frac{-j\varepsilon_0\omega_p^2}{\omega - j\nu}\ . \tag{2.59}$$

The electric permittivity defined by equation 2.53 is found to be

$$\varepsilon = \varepsilon_0 - j\left(\frac{-j\varepsilon_0\omega_p^2}{\omega(\omega - j\nu)}\right) = \varepsilon_0\left[1 - \frac{\omega_p^2}{\omega(\omega - j\nu)}\right], \tag{2.60}$$

which may be expanded into its real and imaginary parts to yield

$$\varepsilon = \varepsilon_0\left(1 - \frac{\omega_p^2}{\omega^2 + \nu^2}\right) - j\varepsilon_0\left(\frac{\nu}{\omega}\frac{\omega_p^2}{\omega^2 + \nu^2}\right). \tag{2.61}$$

In contrast to the collisionless case, the permittivity in the collisional plasma is complex, resulting in phase shift and attenuation of an incident electromagnetic wave. Recalling the relation

$$\beta = \sqrt{\frac{\varepsilon}{\varepsilon_0}}\frac{\omega}{c}$$

and substituting the value of permittivity from equation 2.61 allows a complex propagation constant to be defined. This may be written in terms of real and imaginary dielectric constants:

$$\mu = \mathrm{Re}\left(\sqrt{\frac{\varepsilon}{\varepsilon_0}}\right) \tag{2.62}$$

$$\chi = \mathrm{Im}\left(\sqrt{\frac{\varepsilon}{\varepsilon_0}}\right) \tag{2.63}$$

where the values of χ and μ are found from equation 2.61 as

$$\mu = \left\{ \frac{1}{2}\left(1 - \frac{\omega_p^2}{\omega^2 + \nu^2}\right) + \frac{1}{2}\left[\left(1 - \frac{\omega_p^2}{\omega^2 + \nu^2}\right)^2 + \left(\frac{\nu}{\omega}\frac{\omega_p^2}{\omega^2 + \nu^2}\right)^2\right]^{1/2} \right\}^{1/2} \tag{2.64}$$

$$\chi = \left\{ -\frac{1}{2}\left(1 - \frac{\omega_p^2}{\omega^2 + \nu^2}\right) + \frac{1}{2}\left[\left(1 - \frac{\omega_p^2}{\omega^2 + \nu^2}\right)^2 + \left(\frac{\nu}{\omega}\frac{\omega_p^2}{\omega^2 + \nu^2}\right)^2\right]^{1/2} \right\}^{1/2} \tag{2.65}$$

There is no longer an abrupt change in transmission for frequencies greater than or less than the plasma frequency as with the collisionless case. Figures 2.5 and 2.6 show the refractive and attenuation indices for several different cases using equations 2.64 and 2.65. In the particular case of $\nu > \omega$ and $\omega_{\mathrm{p}} > \omega$, note that the refractive index can be greater than one. Also note the more gradual change in attenuation near $\frac{\omega_{\mathrm{p}}}{\omega} = 1$ for the more highly collisional plasma. This differs markedly from the form given by equation 2.55 for the collisionless case.

For bounded plasmas, or any other conductive medium, microwave attenuation leads to a finite penetration depth. Following the derivation of equation 2.8, it can be seen that finite conductivity adds another term, resulting in the new form

$$\nabla^2 \mathbf{E} - \mu\varepsilon \frac{\partial^2 \mathbf{E}}{\partial t^2} - \mu\sigma \frac{\partial \mathbf{E}}{\partial t} = 0\,. \tag{2.66}$$

Considering only a wave of a single frequency, ω, and assuming a plane wave of amplitude A propagating along the z axis, the following simplified form is realized:

$$-\beta^2 \mathrm{A} + \omega^2 \mu\varepsilon \mathrm{A} - j\omega\mu\sigma \mathrm{A} = 0\,. \tag{2.67}$$

This can be solved for the new propagation constant

$$\beta = \sqrt{\omega^2 \mu\varepsilon - j\omega\mu\sigma} = \sqrt{\omega^2 \mu\varepsilon\left(1 - j\frac{\sigma}{\omega\varepsilon}\right)}\,. \tag{2.68}$$

Equation 2.68 can be separated into real and imaginary parts. The imaginary part, which arises due to the finite conductivity, implies an exponential decay of the incident wave. For a good conductor, this may be defined as a conductor with conductivity satisfying the relation

$$\frac{\sigma}{\omega\varepsilon} \gg 1, \tag{2.69}$$

equation 2.68 can be simplified as

$$\beta = \sqrt{-j\omega\mu\sigma} = \sqrt{\frac{\omega\mu\sigma}{2}} - j\sqrt{\frac{\omega\mu\sigma}{2}}\ . \tag{2.70}$$

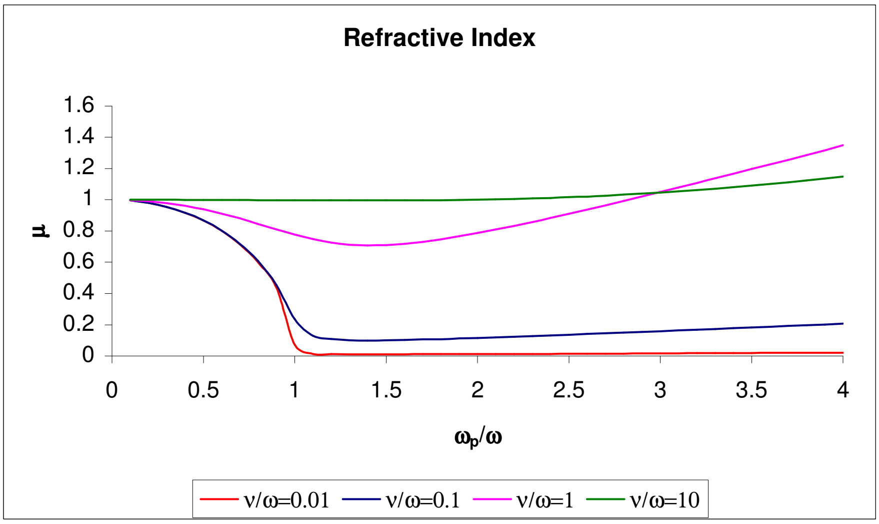

Fig. 2.5: Refractive index for various collision frequencies.

Because the propagation constant has units of inverse length, a skin depth may be defined as

$$\delta_s \equiv \sqrt{\frac{2}{\omega\mu\sigma}}, \tag{2.71}$$

where one skin depth corresponds to the penetration depth at which the field amplitude falls to e^{-1} of its original value. Since the real and imaginary parts have equal magnitude, this distance also corresponds to one wavelength in the conducting medium.

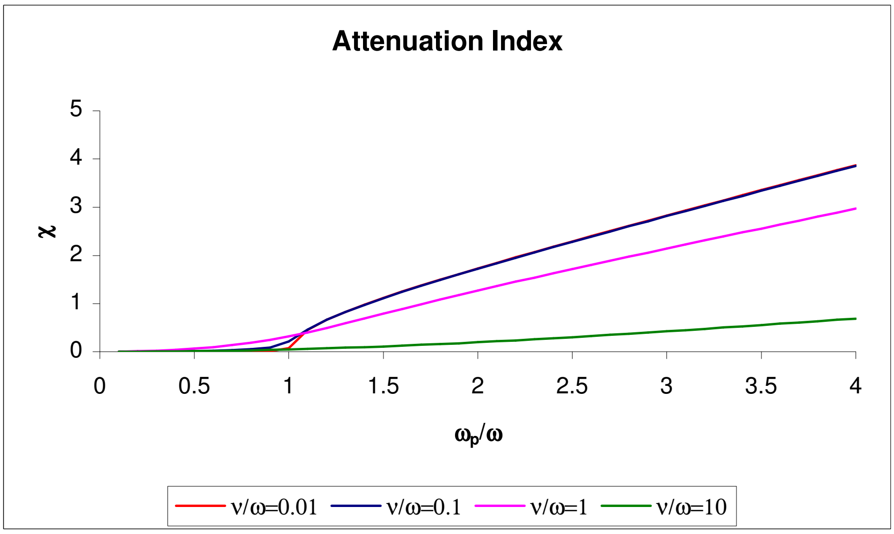

Fig. 2.6: Attenuation index for various collision frequencies.

Most metals behave as good conductors at microwave frequencies. For microwaves at 2.45 GHz, the frequency used in most of the experiments, the skin depth of copper and aluminum is less than 2 μm. The conductivity of plasmas, however, may vary over a wide range depending on the density and collision frequency. In plasmas for which inequality 2.69 is not satisfied, the above simplification is not possible. The conductivity, given by 2.59, is also complex. The propagation constant derived from equation 2.68 then becomes

$$\beta = \sqrt{\omega^2 \mu_0 \varepsilon_0 \left(1 - \frac{\omega_p^2}{\omega^2 + \nu^2}\right) - j\frac{\omega \mu_0 \varepsilon_0 \nu \omega_p^2}{\omega^2 + \nu^2}}\,, \tag{2.72}$$

and can be separated into its real and imaginary components to yield the spatial frequency and attenuation constant, respectively:

$$\mathrm{Re}(\beta) = \left\{\frac{1}{2}\omega^2 \mu\varepsilon\left[\left(1 - \frac{\omega_p^2}{\omega^2 + \nu^2}\right) + \sqrt{\left(1 - \frac{\omega_p^2}{\omega^2 + \nu^2}\right)^2 + \left(\frac{\nu}{\omega}\frac{\omega_p^2}{\omega^2 + \nu^2}\right)^2}\right]\right\}^{1/2} \tag{2.73}$$

$$\mathrm{Im}(\beta)=\left\{\frac{1}{2}\omega^2\mu\varepsilon\left[-\left(1-\frac{\omega_p^2}{\omega^2+\nu^2}\right)+\sqrt{\left(1-\frac{\omega_p^2}{\omega^2+\nu^2}\right)^2+\left(\frac{\nu}{\omega}\frac{\omega_p^2}{\omega^2+\nu^2}\right)^2}\,\right]\right\}^{1/2} \tag{2.74}$$

These are equivalent to equations 2.64 and 2.65, showing the equivalence of complex permittivity and complex conductivity. As in the case of a conductor with a real conductivity, the skin depth of a plasma is the reciprocal of Im(β).

2.3 Microwave Propagation in Plasmas

Ideally, microwave transmission through a plasma may be expressed as a function of the microwave frequency, the path length through the plasma, and the permittivity of the plasma. First two quantities are easily determined. After making a few general assumptions as to the nature of the plasma, a dispersion relation between the permittivity and the relevant plasma parameters may then be decided upon. The Asher-Appleton-Hartree dispersion relation for extraordinary waves propagating across a magnetic field[xiv] was chosen. This relation is the following:

$$\begin{aligned}\varepsilon &= (\eta-i\chi)^2\\ &= 1-\cfrac{w_p^2}{1-iv_e-\cfrac{w_b^2}{1-iv_e-w_p^2}}\end{aligned} \tag{2.75}$$

where w_p, w_b, and v_e are the electron plasma, cyclotron, and collision frequency respectively, all non-dimensionalized (divided) by the angular frequency of the diagnostic microwave signal. During experiment it was found that explicit expressions for the refractive index, η, and attenuation constant, χ, are too unwieldy to be of use here Values of η and χ are readily obtainable from given values of w_p, w_b, and v_e. The attenuation constant, χ, may then be used to calculate the attenuation of a wave propagating through the plasma as follows (transmission factor):

$$\frac{P_2}{P_1}=\left(e^{-\chi\frac{\omega}{c}(x_2-x_1)}\right)^2 \tag{2.76}$$

where P refers to microwave power, x refers to distance the signal has propagated, c is the vacuum speed of light, and ω is the angular frequency of the propagating wave. The quantity is squared to convert from attenuation of the electric field to attenuation of signal power.

In this framework, attenuation is due to an imaginary component to the square root of the permittivity as seen in equation 2.75 (χ). This imaginary component can arise from two separate sources. For a collisionless plasma with positive permittivity, the introduction of collisionality results in attenuation through absorption. On the other hand, the permittivity in collisionless plasma (at low frequencies) can also be negative, resulting again in an imaginary square root. Attenuation in this case corresponds to reflection. Increasing collisionality tends to blur the distinctions between these cases.

2.4 Sources of Error in Transmission Measurements

Even if the absorption per unit length of plasma is completely understood, there are other factors that can significantly influence actual measurements. These will be briefly discussed here:

> Reflected microwaves from the plasma and the microwave horns can interfere with each other during the measurements. It is important to note that transmission measurements, as interpreted by the bulk absorption of the plasma, do not take into account reflection of microwaves due to abrupt changes in the permittivity at plasma boundary. Furthermore, in a manner similar to an optical etalon, standing waves can build up between the abrupt changes in refractive index encountered at the microwave horns, at the plasma edges, and at the walls of the discharge cell. The fraction of microwave energy coupled out of the system will be affected by both changes in the attenuation index, and the refractive index. In our case, this effect is increased by the fact that the microwave horns are connected to the plasma via the stainless steel magnet bore. A large fraction of the microwave power reflected from the plasma will then reach the launching horn, and likewise, microwave power reflected from a microwave horn will propagate back to the plasma.
>
> Refraction and diffraction of the diagnostic wave front across the plasma can contribute to the focusing of the microwaves and can interfere with measurements of both microwave transmission and

path length. In this investigation, a 0.5” orifice plate was placed just past the plasma in an attempt to select out only the portion of the wavefront that passed through the plasma. However, the intensity and relative phase of the microwaves impinging upon this hole will still affect the amount of microwave energy that gets through the hole.

While the previous two arguments are qualitative, it was observed changes of the order of 80% in measured transmission corresponding to relatively small changes in the placement of the microwave horns. Similar effects have been observed[xv] and explained in other microwave transmission setups.

These effects are typically avoided by selecting a diagnostic frequency with a wavelength much less than the plasma length scale, and far from any resonance or absorption. This results in a refractive index close to unity. Using such a method requires a long path length over which a measurable effect may be integrated. In our case, the path length through the plasma will be shown to be on the order of one vacuum wavelength of the plasma frequency. To obtain a measurable effect, therefore, our diagnostic frequency must be close enough to the plasma frequency such that the above sources of error can no longer be neglected.

2.5 Non-Transmission

While measurements of a particular transmission fraction are prone to uncertainty, we claim that the measurement of zero transmission is quite reliable and particularly useful in a finite plasma. In our system, we can confidently claim that for a non-transmitting plasma, we will not observe transmission through our system. Such a measurement is not changed by the various wave effects, reflections, and impedance issues that strongly influence a measurement of transmission fraction through a small, three dimensional plasma. This is complemented by the fact that significant changes in the refractive index that could also eliminate transmission via reflection are concurrent with a significant decay of a propagating signal.

Zero transmission refers to either a resonance, at $\mu = 0$, or a cutoff, at $\mu = \infty$. In the case of a collisionless plasma, these conditions both correspond to complete reflection and are easily solved for from equation 2.75, Cutoff

$$w_p^2 = 1 \pm w_b \tag{2.77}$$

Resonance

$$w_p^2 = 1 - w_b^2 \tag{2.78}$$

Fig. 1.7 shows the resultant Clemmow-Murray-Allais, or CMA diagram, depicting zones of transmission and the lack of a mode of extraordinary microwave transmission.

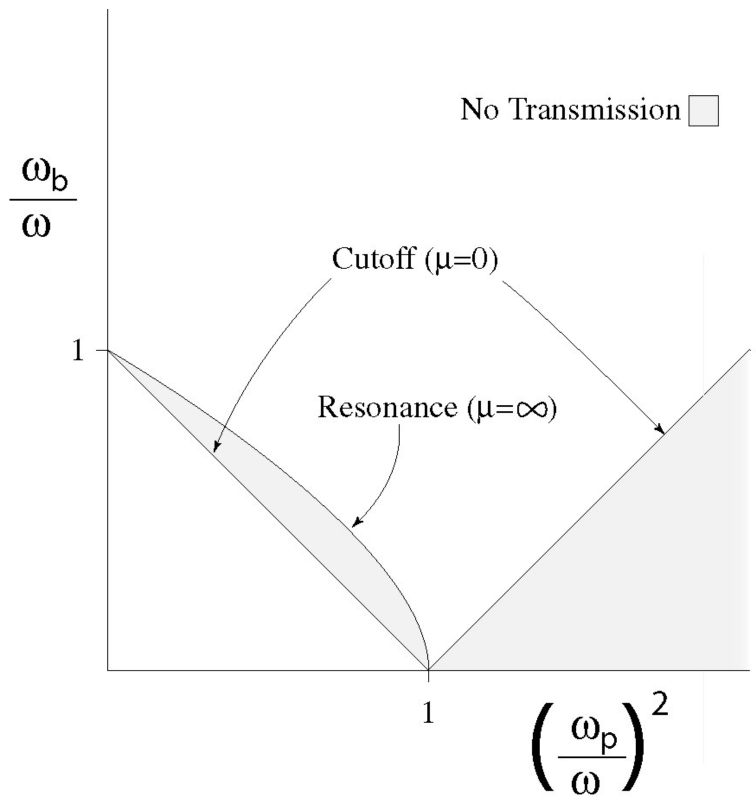

Fig. 1.7: CMA diagram for extraordinary waves through a magnetized plasma.

Although this plot assumes a collisionless plasma, it does give insight as to where regions of interest might be located, in particular the zone of zero transmission to the left of Fig. 1.7. This band is referred to as the upper hybrid resonance, so called because its frequency corresponds to the sum, in quadrature, of the plasma frequency and the cyclotron frequency.

Collisionality affects transmission through the plasma in several ways. Most significantly in our case, collisionality reduces the depth of upper hybrid resonance band when scanned far from the plasma frequency ($\omega_p/\omega < 1$). This is unfortunate, because taking Fig. 1.7 at face value, one could, in theory, use an arbitrarily high diagnostic frequency ($\omega_p/\omega \sim 0$) and perform measurements near $\omega_p/\omega = 1$. Using such a high frequency (short wavelength) diagnostic would, in turn, make our plasma relatively large and mitigate many of the problems associated with measurements of the transmission fraction.

3. Experimental Accessories

3.1 Magnet

The magnet used was an Oxford Instruments NiTi, split pair system with three optical axes (bores). A maximum field of 6.5 Tesla is attainable with the system. The field is designed to be uniform over a 7.62 cm^3 at the center of the three bores which are 7.62 x 8.89 cm parallel to the field, 7.62 x 7.62 cm perpendicular to the field and horizontal (the wind-tunnel bore), and 3.81 cm diameter vertical (the microwave diagnostic bore).

3.2 High Voltage Pulser

The non-equilibrium plasma is sustained via a custom Russian made high repetition rate, high voltage, short pulse duration electrical pulser. The device uses an L-R-C circuit along with the switching characteristics of a diode to create 2 ns, high-voltage, 25 Ω, pulses at a maximum repetition rate of 100 kHz. Using a 3 x 75Ω cable transformer with an effective output impedance of 225 Ω, the pulser is then capable of generating a 30 kV pulse across a 400 Ω load.

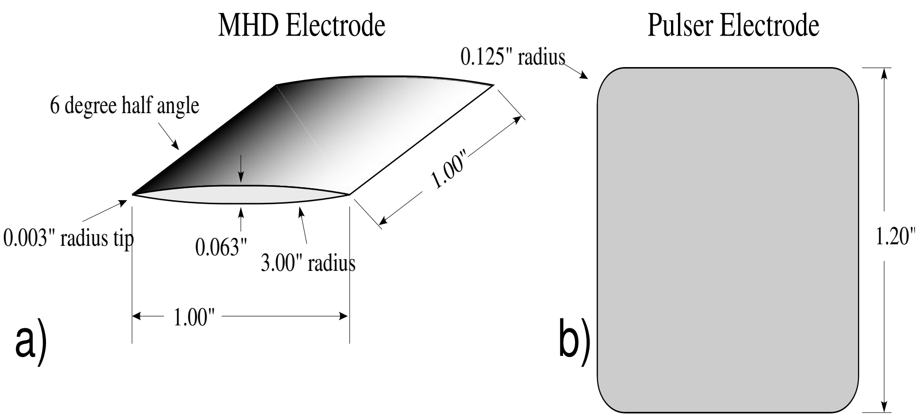

Fig. 3.1: Schematic of MHD electrodes for power addition/extraction (a), and pulser electrodes for sustaining conductivity (b).

3.3 Mach 3 Flow

Mach 3 flow is achieved through a converging/diverging nozzle, the contour of which was taken from an existing wind-tunnel at the Princeton University

Gas Dynamics Laboratory operating at a similar Reynolds number. The test cross-section measures 3 cm x 5 cm. Because of its optical clarity, resistance to abrasion, electrical insulation, and mechanical properties at high temperatures, polycarbonate was used for the tunnel construction.

The tunnel is run in an in-draft setup using an air ejector pump to maintain the low back pressure. The plenum pressure is throttled down to 450 Torr resulting in laminar flow through the test section with static conditions of 10 Torr and 106 Kelvin at a velocity of620 m/sec.

3.4 The Static Cell

The static discharge cell was a rectangular box constructed from 9.52 mm polycarbonate sheet. The cell measured 20.32 cm in length with a 3.05x5.08 cm interior cross-section. One end of the cell was sealed to a vacuum system, and the other end was connected to an air intake with a needle valve. The desired pressures of 1, 5, 10, and 20 Torr were then obtained by throttling the intake with the needle valve. This also provided for a throughput of air to sweep out impurities. The discharge was drawn along the magnetic field lines between two flat, 7.62x3.05 cm aluminum electrodes on the sidewalls.

Because the discharge is drawn along the magnetic field, the magnetic field intensity has very little effect on the discharge parameters. This is verified visually, and electronically by monitoring the voltage and current levels of the discharge. Furthermore, due to the pulsed nature of the discharge, when it is 'on' the current density is several orders of magnitude beyond the normal current density. This causes the discharge to use the entire cathode, essentially fixing the current density.

3.5 Microwave System

To ensure repeatability, experiments were performed using two microwave diagnostic frequencies. The first frequency of 12.6 GHz was chosen based on the geometry of the setup and preliminary estimations of the plasma properties. The 2nd frequency of 18.5 GHz was chosen based on results using the first frequency. Both sources had a maximum power around several milliwatts which is well below the power required to perturb our plasma significantly. To remove any possible influence of the magnetic field on the microwave oscillators, the oscillators were placed three meters from the magnet in a ferromagnetic steel box. The microwave signals were transmitted to and from the experiment using low-loss LMR-240 coaxial cable. As shown in figure 3.2, the microwave signal was then broadcast from a WR-112 horn into the vertical bore of the magnet. A 12.7 mm aluminum orifice plate was placed after the discharge cell to select out only the portion of the wave front that passed through the discharge. Following the path of the microwaves shown in Fig. 3.2, the transmitted signal then passed through the rest of the magnet bore, into the WR-112 receiving horn, into a 27 dB amplifier, into a HP crystal detector, and finally into a 50 Ω terminated 400 MHz digital oscilloscope.

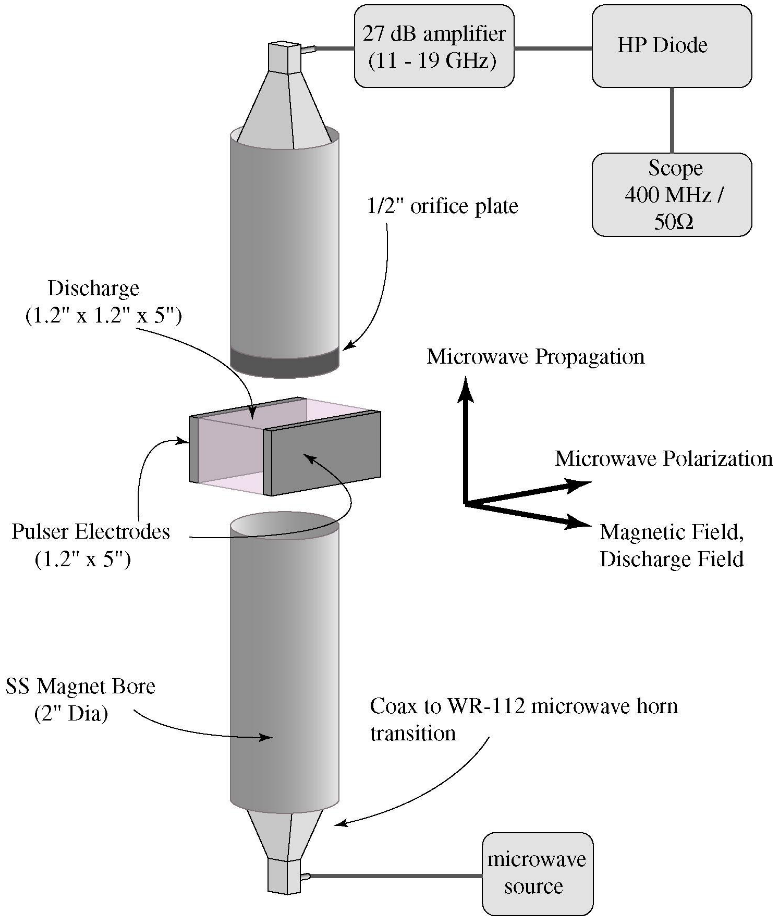

Fig. 3.2 : Schematic of the experimental layout.t

Polarization was observed to be maintained through our system. Rotating the WR-112 horns perpendicular to one another caused the signal to drop to less than 2% of its maximum (horns parallel) value. This in spite of the fact that our diagnostic frequencies of 12.6 and 18.5 GHz are well outside of the 7 to 10 GHz range for which such horns are designed. Because the polarization will be shown to be critical to this experiment, we take the uncertainty in the measured transmission fraction to be 2%.

To verify that microwave energy would not be conducted around a non-transmitting plasma, two test pieces were constructed, one from aluminum and the other from graphite. The test pieces were fabricated to the same dimensions as the plasma. Inserting either of these test pieces to the same location as the plasma caused the measured microwave transmission to vanish.

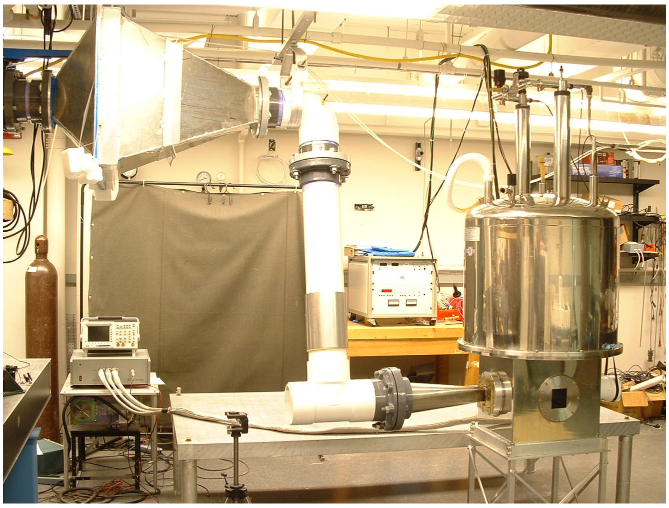

Fig. 3.3: Superconducting Magnet along with the Test Facility.

3.6 Electrode Setup

All electrodes were machined from aluminum jig plate. This was done for two reasons: Firstly, jig plate is dimensionally stable for machining shapes with high aspect ratios. Secondly, in air, aluminum has the lowest cathode voltage drop of any common structural material[ix] (Although this latter fact will be discussed shortly and shown to be inconsequential). A schematic of the pulser electrodes, through which the plasma was sustained, is shown in figure 3.1b.

In previous experience, three-dimensional corners were found to create sufficient heat to deteriorate the polycarbonate tunnel walls. For this reason, the corners of the pulser electrodes are rounded. The electrode geometry was arrived at through an iterative approach. A large plasma volume is desired, but because of the large density gradients (and associated conductivity gradients) across a supersonic flow, wider electrodes allow the discharge current to flow mostly through the boundary layer. In the stream-wise direction, the plasma need only be as long as the power extraction/addition electrodes. Any unnecessarily increased length in this direction needlessly heats the flow and increases the power load on the pulser.

The design of the MHD power extraction electrodes, which will henceforth be referred to as the MHD electrodes, has three main constraints:

1) The MHD electrodes must be in contact with the conductive plasma. Because the discharge is in the free stream flow, these electrodes must extend from the tunnel wall into the discharge.
2) The MHD electrodes must not short out the pulser sustained discharge. Their (span-wise) thickness must be small relative to the tunnel width, otherwise the pulser sustained discharge will be diverted from the supersonic flow into the MHD electrodes leaving a void in conductivity between the electrodes.
3) Their impact on the fluid flow should be minimal. Along with the second condition , this suggests a low profile wing geometry.

The resultant MHD electrode design is shown in figure 3.1a.

3.7 MHD Current Measurement Setup

Electrical noise from the pulser, combined with the interaction of the pulser electrodes and the MHD electrodes as coupled through the discharge pose difficult challenges in measuring the Faraday current. For an ideally balanced pulser discharge, the pulser anode and cathode would receive equal and opposite positive and negative voltages respectively. Unfortunately, this is not observed. Due mainly to asymmetric capacitive coupling of the pulser electrodes and their various connecting lines to the ground, the MHD electrodes float up and down many kilovolts during a 2ns pulse. Because of the great disparity in this voltage swing relative to the expected MHD voltage/current characteristics, filtering is not feasible. The solution is to isolate the MHD electrodes (and associated measurement circuit) from ground and to minimize the capacitance of the circuit relative to both ground and to free space, and to maximize its impedance to the short, high-voltage pulse. A small circuit was constructed using an LED to measure Faraday current and to achieve optical isolation. A second diode was added to protect the LED from reverse voltages. A resistive bridge was used to provide a bias voltage across the channel with the intent, at the time, of overcoming the cathode sheath voltage. The resistance bridge also provides isolation between the MHD electrodes and the laboratory.

The device was calibrated by connecting a function generator in parallel with the MHD electrodes. Current was determined by measuring the voltage across one of the 2kΩ resistors with an oscilloscope. This was compared to the output of the PMT as measured on an oscilloscope. The LED/PMT circuit was found to have a threshold of 75 µA, a sensitivity of 20 mV/ma, and, aside from propagation delay, a frequency response in excess of 100 MHz.

3.8 Discharge Current Measurement Setup

The discharge current through the pulser electrodes was measured by placing a 1.2 Ω shunt (consisting of ten 12 Ω, low inductance, carbon resistors) in series with the pulser as shown in figure 3.4. This setup measures both displacement and conductive current through the channel.

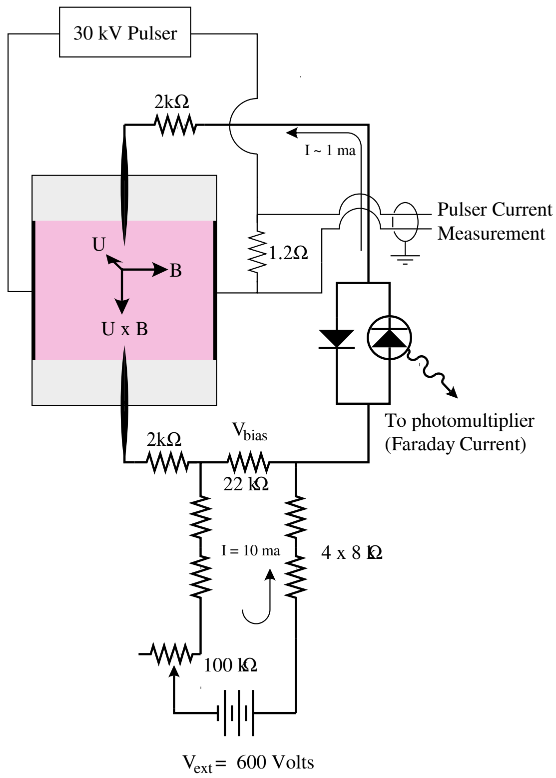

fig. 3.4: Diagram of discharge current and Faraday current measurement setup.

3.9 Imaging

A Fuji 2800 CCD camera was used to record images of the discharge in the MHD channel. CCD cameras have been found to be resistant to magnetic fields of the order of one Tesla and to electrical noise generated by the pulser.

The camera has a 6x optical zoom allowing it to be placed a safe distance from the magnet. The camera was positioned downstream of the test section looking directly upstream to the discharge through an acrylic window.

4. Results & Discussion

4.1 Relevant Parameters

In all experiments presented in this work the magnetic field used was 5 Tesla. If an electron collision frequency of 4 GHz per standard Torr is assumed[ix] the resultant Hall parameter at our test section conditions is $\Omega_e \approx 7$. In the boundary layer where the density is approximately three times lower than in the Mach 3 flow, the Hall parameter will be on the order of 20. Since the following relation gives the ratio of the conductivities along and across the magnetic field lines,

$$\sigma_{\perp} = \sigma_{\parallel} \Big/ \left(1 + \Omega_e^{\ 2}\right), \tag{4.1}$$

where $\sigma_{\parallel}$ and $\sigma_{\perp}$ are the conductivities parallel to and perpendicular to the magnetic field respectively, then we expect a huge disparity when comparing conductivities between the MHD electrodes to conductivities between the pulser electrodes. The magnetic field is therefore expected to have a dramatic effect on the current path of the discharge. A further consequence of the tensor nature of the conductivity is to increase the effective area of the MHD electrodes by allowing them to draw Faraday current from a wider area of the plasma than their cross section would suggest.

The flow time through the MHD channel, which is taken to be the time it takes for the free stream flow to convect over the pulser electrodes, works out to be 42 μsec. This corresponds to four of the 100 kHz high-voltage pulses.

Theoretical prediction over the properties of the experimental MHD channel can be found on figure 4.0. However, some strong deviations from those have been observed. Budgetary and time constraints necessitate a relatively small scale experimental facility. This will tend to reduce results for three reasons:

Sheaths – While the voltage of the MHD generator (uBd) varies linearly with length, the cathode voltage drop does not. In this experiment uBd is 600 m/s x 5Tesla x 5 cm = 150 volts, which is smaller than the cathode drop from aluminum in air of 230 volts[ix]. Whereas in a large-scale facility this voltage drop would be small or negligible with respect to the Faraday EMF, it is a dominant feature in this experiment.

The length of the interaction region in this experiment is a couple of centimeters. This reduces the aspect ratio of the channel making segmentation and Hall setups difficult. The fraction of energy removed from a given flow is proportional to the length of the channel.

In low Reynolds number wind-tunnel flows, the boundary layer comprises a relatively large fraction of the flow-field. Dealing with large boundary layers and their associated conductivity gradients complicates the design of an MHD channel.

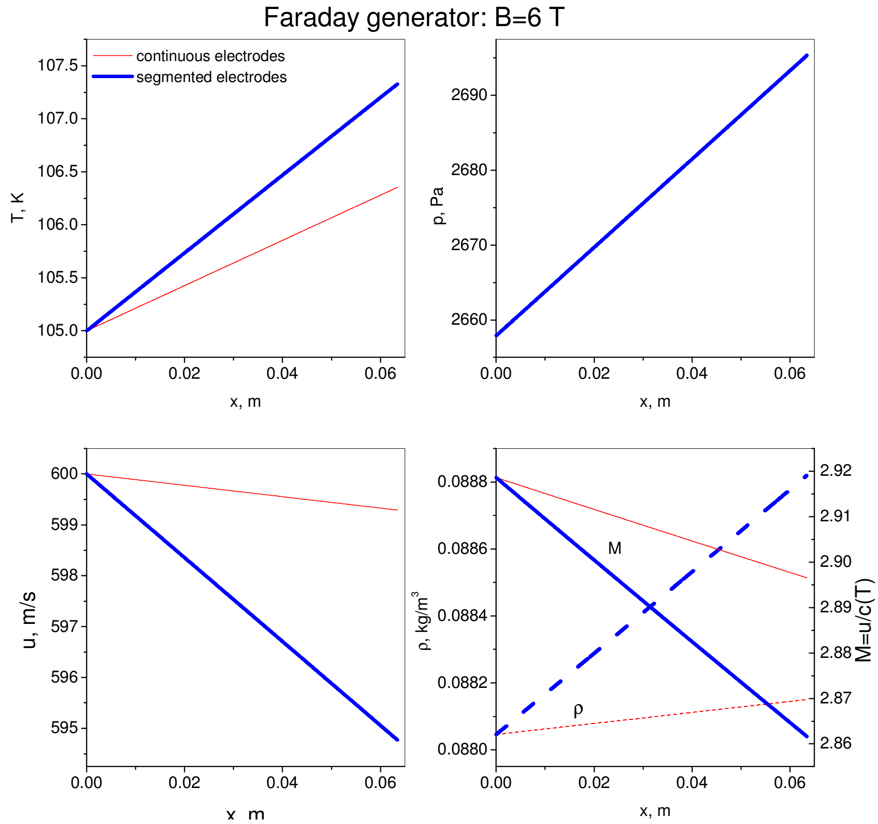

Fig. 4.0: Predictions for Faraday Generator with continuous and segmented electrodes. B = 6 Tesla, <ne>=5×10^{11} cm^{-3}; K (loading factor) = 0.5.

<u>4.2 Images of Discharge</u>

A progression of images of the discharge is shown in figure 4.1 along with scaled sketches of the MHD channel cross section. The images were taken from downstream of the MHD.

In figure 4.1a corresponds to the first and simplest channel design. In this case the pulser electrodes span the full height of the wind-tunnel walls.

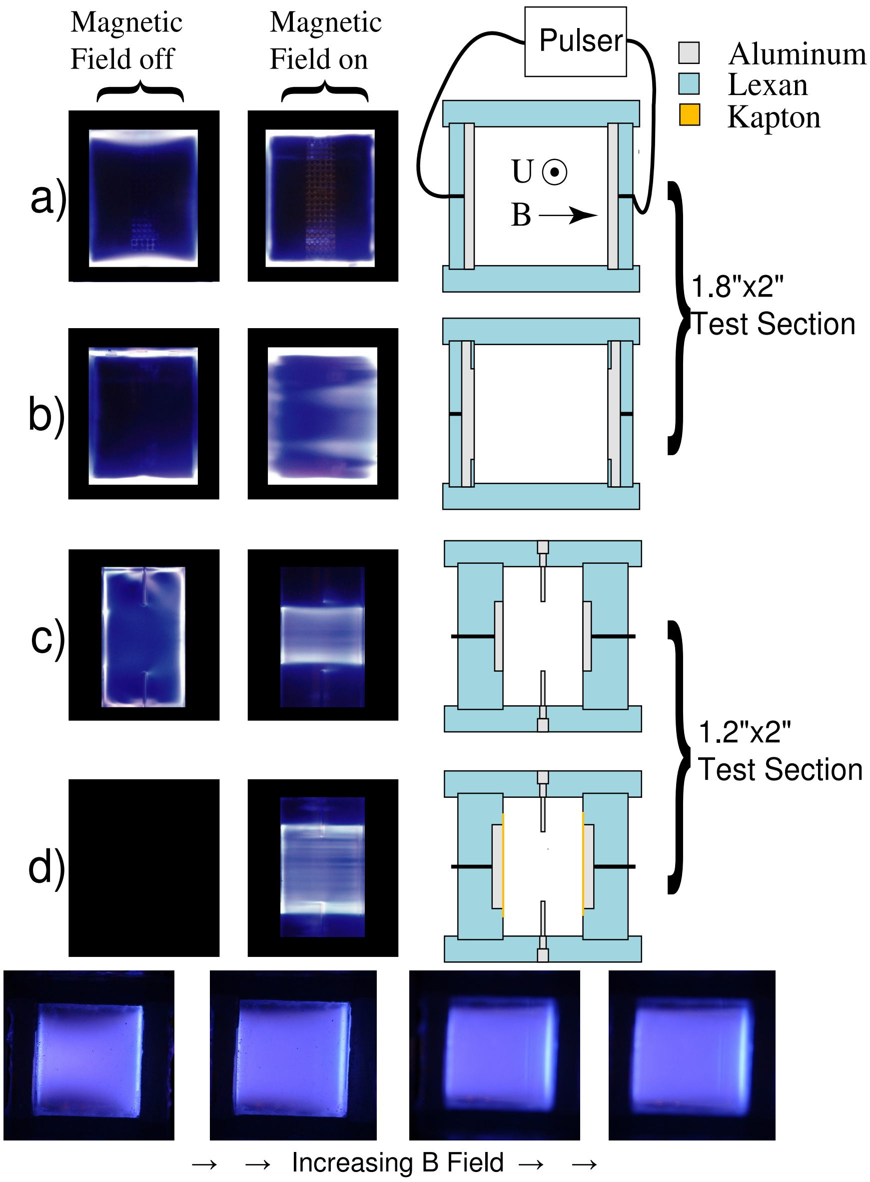

Fig. 4.1: The iteration of MHD channels from the first setup (a) with the plasma entirely in the boundary layer, to the present setup (d) with the plasma volume filling and in the supersonic core flow.

It is clear that the entire discharge is confined to the boundary layer. The bulge seen in the plasma in the top left image (without the magnetic field) is consistent with the form of the boundary layer of a rectangular supersonic wind-tunnel in what is often referred to as the "dog bone" form of the free stream flow. As expected, applying a magnetic field has the effect of confining the current path to the magnetic field lines and, in this case, reducing its fraction in the free stream.

Figure 4.1b shows the second iteration in the development of the MHD channel. In this case portions of the electrodes over the floor and ceiling boundary layers are insulated with a 1cm wide layer of 2mm thick polycarbonate dielectric. The luminous portion of the discharge is still primarily in the boundary layer. However, the effect of the applied magnetic field is evident to cause a significant amount of the discharge to be confined to the volume between the pulser electrodes.

As shown in figure 4.1c, the pulser electrodes were narrowed further in an attempt to remove the discharge entirely from the floor and ceiling boundary layers. The thin profile, wing cross section electrodes described in figure 3.1 were introduced to measure Faraday current. Once again, the effect of the magnetic field is seen: in this case removing the discharge entirely from the boundary layer and into the free stream.

The final design of the channel is shown in figure 4.1d. In this case the pulser electrodes were widened so as to ionize a greater fraction of the flow (60% of the flow passes through the discharge). The Faraday electrodes are now bathed in the plasma with a clear conductive path through the high velocity flow. The additional step of covering the pulser electrodes with Kapton tape was implemented to insure that the Faraday current was not shorted out. This is necessitated by the fact that due to the Hall parameter of 7, the conductivity along the magnetic field (between the Faraday electrode and the pulser electrode and back) is roughly 50 times the conductivity between the electrodes. The nude pulser electrodes effectively neutralize all vertical electrical fields in the discharge.

Horizontal layers of varying brightness are seen in all instances of the discharge with the magnetic field on. These are currently a subject of investigation.

4.3 Pulse Current and Voltage

The resistive shunt used to measure the discharge current supplied by the pulser was presented in the previous chapter. To determine the approximate impedance of the plasma, resistors were placed in series with the pulser electrodes with one atmosphere of air in the wind-tunnel test section (sufficient to prevent breakdown). Time traces of the resulting voltages were recorded on an oscilloscope. Oscilloscope traces corresponding to several resistor values were compared to traces corresponding to breakdown through the Mach 3 flow.

Visual analysis of shunt signals shows that after breakdown the resistance of the discharge is approximately 1 kΩ (relative to the pulser).

For an ideal cable transformer carrying a pulse of 225 Ω 30 kV, we would expect the voltage peak at the pulser electrodes to be nearly 60 kV. However, due to capacitive coupling between the electrodes, their connections to the cable transformer, the magnet body, and free space, the actual voltage across the pulser electrodes is estimated to peak at approximately 30 kV. This corresponds to a discharge current of less than 30 A through the equivalent 1 kΩ resistance.

4.4 Faraday Current & Voltage

The principle employed to measure Faraday current was as follows: The MHD channel was run with the magnetic field set to 5 Tesla. PMT voltage traces corresponding to Faraday current were recorded on an oscilloscope. Because the circuit (shown in figure 3.4) is only sensitive to current flow in one direction, the magnetic field direction was then reversed and data was recorded a second time. It was assumed that the form of the pulser driven discharge would be independent of magnetic field direction. It is clear from the images of figure 4.1 that a comparison of the cases of B = 5 Tesla and B = 0 correspond to completely different plasmas and would not isolate the measurement of Faraday current.

This method was employed in all cases shown in figure 4.1. Current vs. time traces of the resultant Faraday current are presented in figure 4.2. Seems that, these curves demonstrate for the first time a cold-air supersonic MHD generator.

Kapton foils have proved to be essential in MHD voltage detection, as with their absence the Faraday field is shortened by pulser electrodes.

To gain further insight into the electrical characteristics of the MHD channel, current measurements were recorded using a variety of bias voltages and are presented in figure 4.3 The cases corresponding to *112* Volts - *UB* and +*UB* are very similar. This implies the Faraday voltage to be 56 Volts. The measured current in the *80* Volts - *UB* case suggests the Faraday voltage is less than 80 Volts, which is consistent with the 56 Volt estimate.

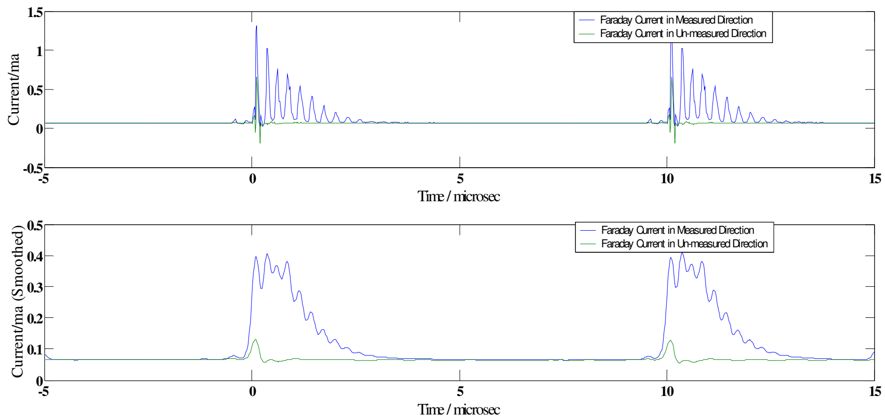

Fig. 4.2: Faraday current measurements with the magnetic field in each direction. In the bottom graph, the plot has been smoothed with a 250 ns Gaussian window.

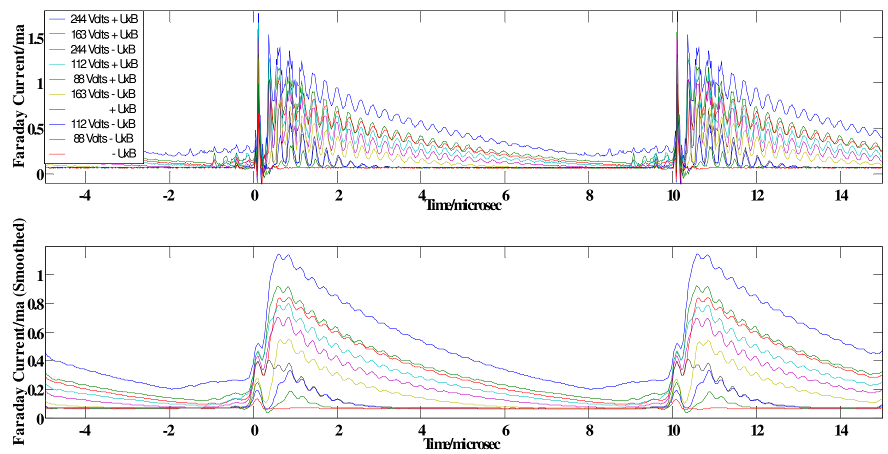

Fig. 4.3: Faraday current measurements with different bias voltages and magnetic field directions. In the bottom graph, the plot has been smoothed with a 250 ns Gaussian window. The order of the curves from top to bottom is the same as the order in the legend.

If the Faraday voltage is assumed to be 56 Volts, and considering the peak currents in figure 4.3 range from 0.4 to 1.1 mA for corresponding voltages ranging from 56 to 300 Volts, then peak conductivities across the MHD generator correspond to resistance levels of 140 kΩ to 270 kΩ. This increase in resistance with increasing current flow is consistent with expectations across a cathode sheath.

Several comparisons with basic theory can be made at this point. The ratio of resistance of the plasma across the magnetic field lines (~200 kΩ) to the resistance along the magnetic field lines (~1 kΩ) is approximately 200. As the Hall parameter ranges from 20 to 7 from boundary layers to the isentropic free stream, from equation 4.1 we would expect the conductivity ratio to be between 400 and 50.

4.5 Microwave Measurements in Static Cell

The transmission fraction of extraordinary microwaves propagating through our system, was measured at an assortment of different magnetic field values. The measurements were performed at both diagnostic frequencies used in this investigation. The results are shown in 4.4 and 4.5. In all cases, the periodic nature of our pulsed ionization scheme is evident with a 10 μsec period. Also in all cases, the system has reached a pseudo-steady state over several seconds. A closer inspection shows that the transmission fractions are not explained by a simple interpretation based on the calculated values in figure 4.6 and figure 4.8. It is possible to attribute this to the refraction, diffraction, reflections, nor impedance mismatching discussed previously.

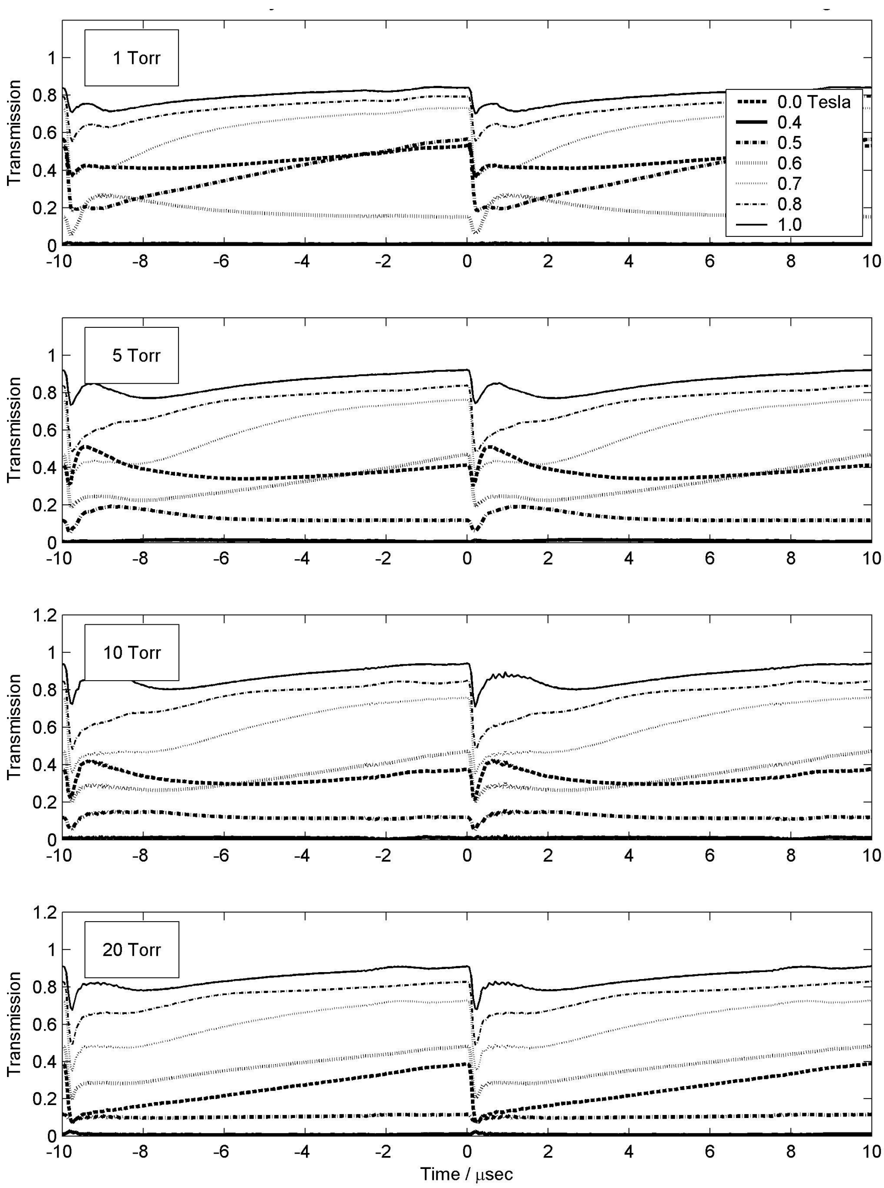

Fig. 4.4: Measured transmission of 12.6 GHz microwave through plasma at the four pressures investigate.

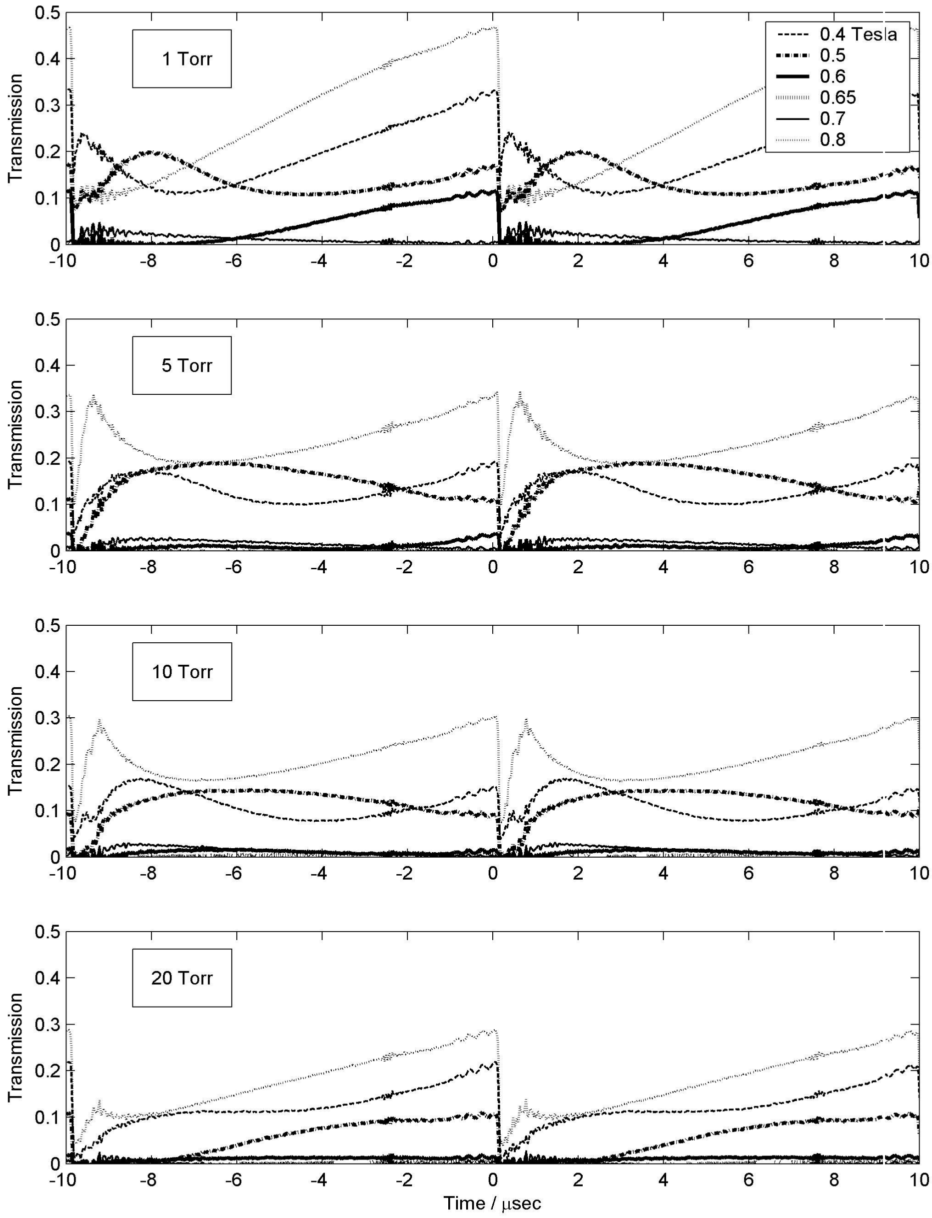

Fig. 4.5: Measured transmission of an 18.5 GHz microwave signal through plasma at the various pressures and magnetic field values investigated.

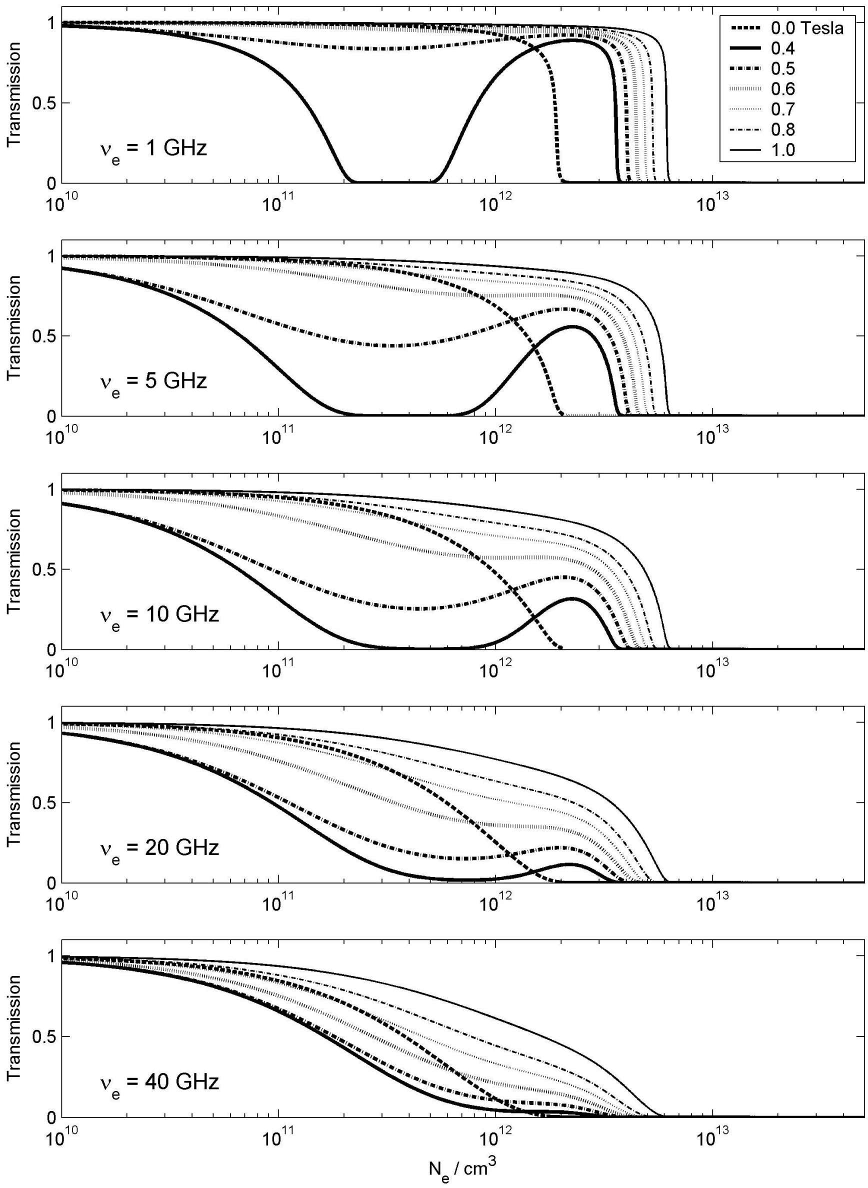

Fig. 4.6: Calculated transmission of 12.6 GHz microwaves through 3 cm of plasma.

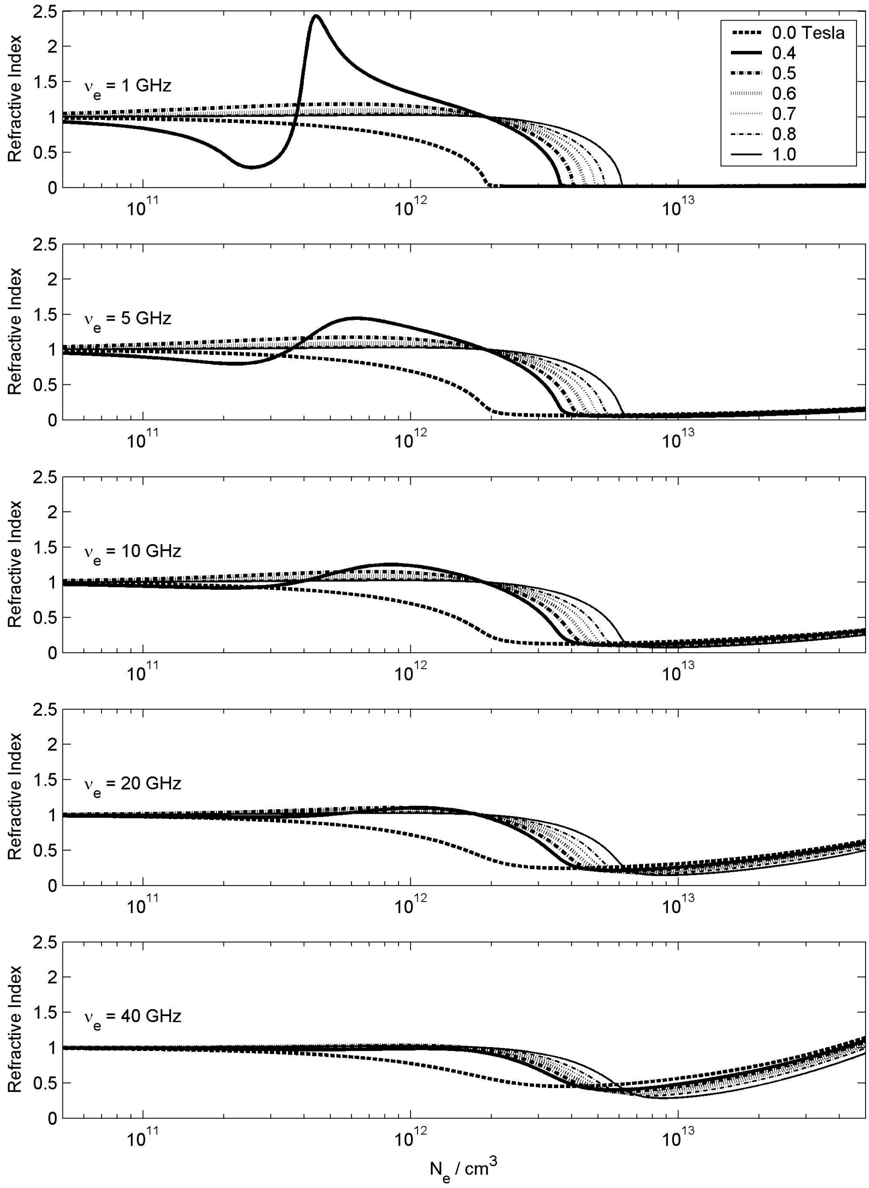

Fig. 4.7: Refractive index for transmission of 12.6 GHz microwaves.

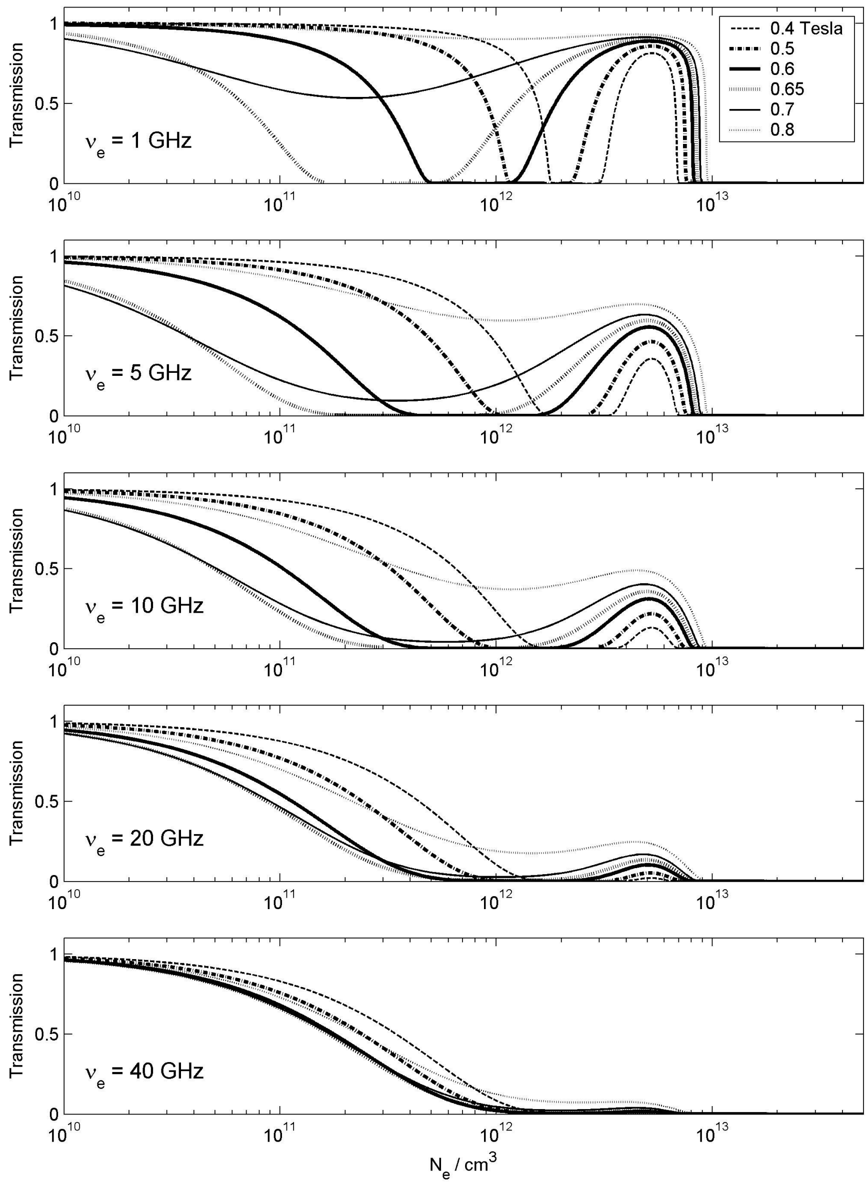

Fig. 4.8: Calculated transmission of 18.5 GHz microwaves through 3 cm of Plasma.

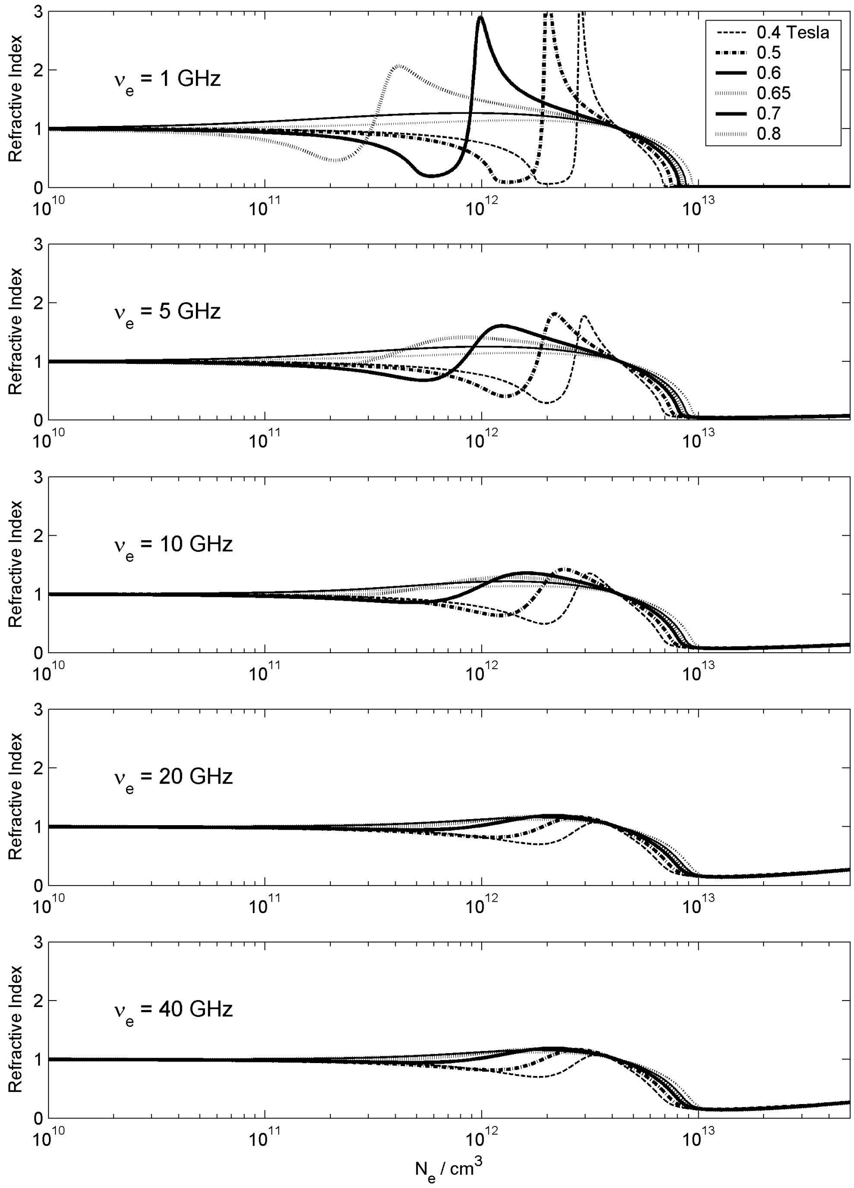

Fig. 4.9: Refractive index for transmission of 18.5 GHz microwaves.

4.6 Emission Spectroscopy

Emission spectroscopy was used to measure the average rotational and vibrational temperatures in the static cell plasma for various pressures. Figure 4.10 shows that the rotational temperature increased from 200 K to about 500 K as the pressure was raised from 1 torr to 20 torr in the static cell. This temperature was measured from several vibrational bands[xvi]. The average vibrational temperature was measured to be around 1141 K.

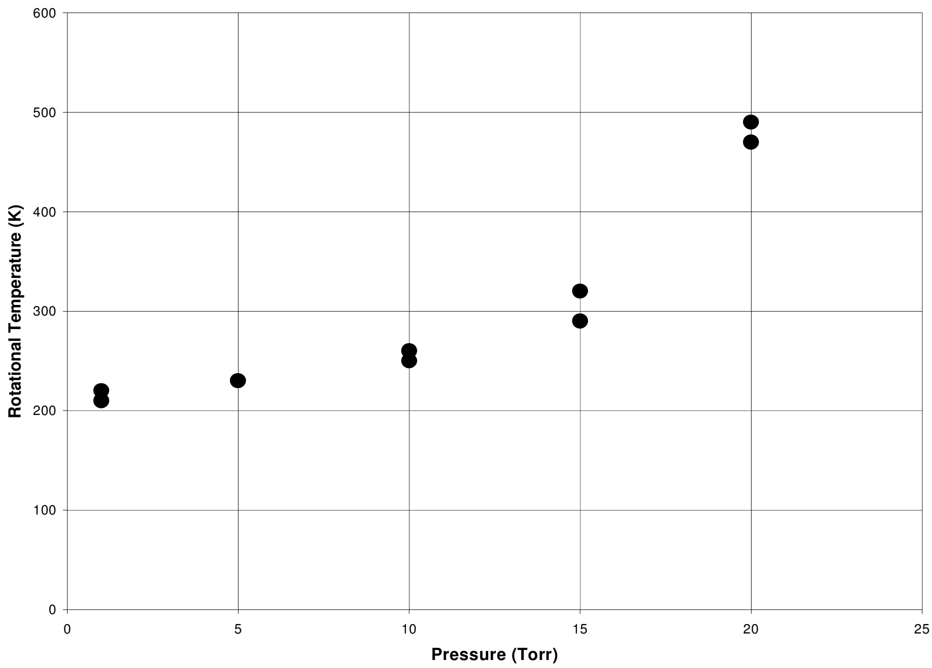

Fig. 4.10: Averaged rotation temperature as a function of static cell pressure (two data set are shown).

4.7 Results and Discussion from Microwave Data Set

A very significant feature can be found in the transmission measurements of 12.6 GHz at 0.4 Tesla in figure 4.4. In this case no transmission is observed at any of the pressures studied. It was then realized that collision frequencies considerably lower than what was first assumed could explain the complete absorption. This, combined with the observed transmission at the other applied field strengths lead to a significant logical conclusion when compared to the calculated transmission values shown in 4.6. The electron number density and electron collision frequency must lie within the following ranges.

$$2\times10^{11}\ \mathrm{cm}^{-3} < n_e < 10\times10^{11}\mathrm{cm}^{-3} \qquad (4.2)$$
$$\nu_e < 20\ \mathrm{GHz} \qquad (4.3)$$

The measurements at 12.6 GHz motivated the next set of data using the 18.5 GHz source. This frequency was chosen, according with the magnetic field intensities, to 'scan' the upper hybrid absorption band through the number density range predicted using the absorption at 12.6 GHz at 0.4 Tesla. The resultant transmission measurements are shown in Fig. 4.5.

There is a wealth of information presented in this figure, particularly when compared with the absorption bands shown in figure 4.8. The lack of transmission of 18.5 GHz at 0.65 Tesla is consistent with the lack of transmission of 12.6 GHz at 0.4 Tesla. Both imply the number density and collision frequency range given in equations 4.2 and 4.3. Here follows all the pressure measurements:

<u>1 Torr:</u>

With an applied field of 0.4, 0.5, and 0.8 Tesla, significant transmission is observed. Initially, at 0.6, 0.65, and 0.7 Tesla no transmission is observed. At 3 μsec, 0.6 Tesla begins to transmit. These observations, viewed in light of the calculated transmission fractions shown figure 4.5***Fig.*** , lead to the conclusion that the electron collision frequency is in the range of 5 to 10 GHz and the electron number density is in the range of $2\text{x}10^{11}/\text{cm}^3$ to $9\text{x}10^{11}/\text{cm}^3$. At 3 μsec the number density falls below the 0.6 Tesla resonances. This happens in the vicinity of $3\text{x}10^{11}$ per cm^3. These number density ranges are shown graphically in figure 4.11.

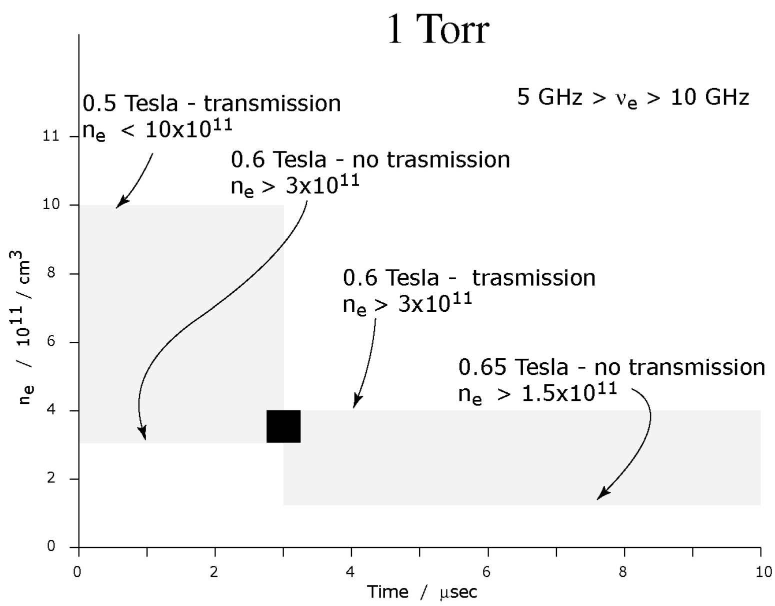

Fig. 4.11: Electron number density for 1 Torr plasma over one 10 μsec pulser cycle.

<u>5 Torr:</u>

The transmission data at 5 Torr is quite similar to the data at 1 Torr. The transmission at 0.6 Tesla begins at about 7.5 μsec (n_e ~ $3\text{x}10^{11}$ per cm^3), and 0.5 Tesla does not transmit at first. This latter observation implies the initial electron number density to be approaching 10^{12} per cm^3. These ranges are shown in figure 4.12.

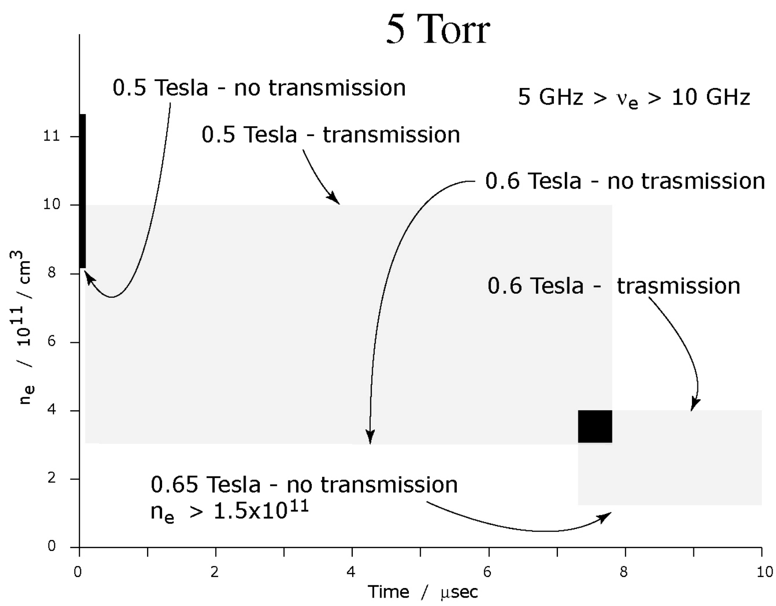

Fig. 4.12: Electron number density for 5 Torr plasma over one 10 μsec pulser cycle.

<u>10 Torr:</u>

This case follows the trend of the previous two cases in that no transmission of the 0.6 Tesla plasma is observed at all. In addition, the 0.5 Tesla plasma also blocks initially. The remaining 9 μsec, in which the 0.5 Tesla plasma transmits while the 0.6, 0.65, and 0.7 Tesla plasmas do not transmit implies that the electron collision frequency is less that 20 GHz. For electron collision frequencies between 5 GHz and 20 GHz, the lack of transmission at both 0.6 Tesla and 0.65 Tesla implies the electron number density to be in excess of $3x10^{11}$ per cm^3. These ranges are shown in figure 4.13.

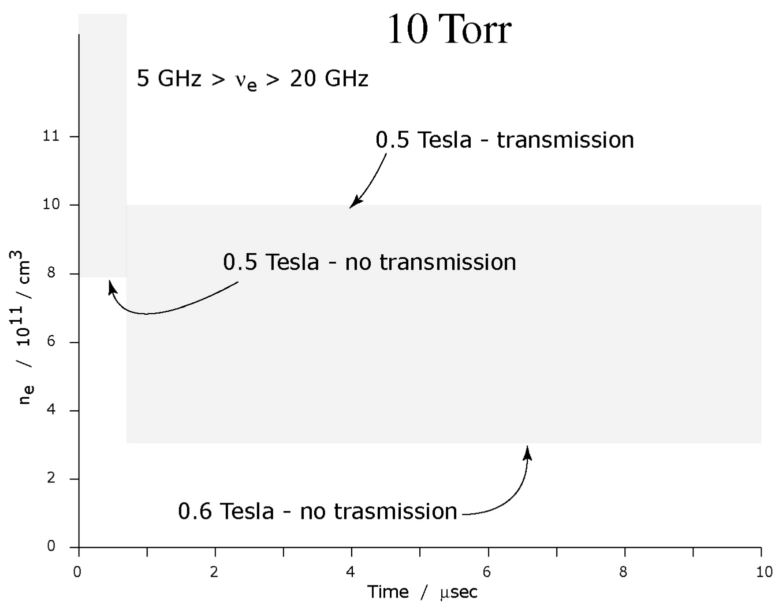

Fig 4.13: Electron number density for 10 Torr plasma over one 10 µsec pulser cycle.

<u>20 Torr:</u>

The conclusions in this case are similar to those in the 10 Torr case, except that here, the 0.5 Tesla plasma does not transmit until nearly 3 µsec. These ranges are shown in figure 4.14.

By means of the high-voltage, short duration, pulsed ionization scheme it was possible to obtain initial electron number densities on the order of 10^{12} per cm^3, and electron collision frequencies in the range of 5 GHz to 20 GHz. The number densities then decayed to 2 to 5 $x10^{11}$ per cm^3 over the 10 µsec delay between high voltage pulses. A trend of increasing number density and collision frequency with increasing pressure is observed. These increases however, are quite modest with respect to the 20 fold increase in pressure.

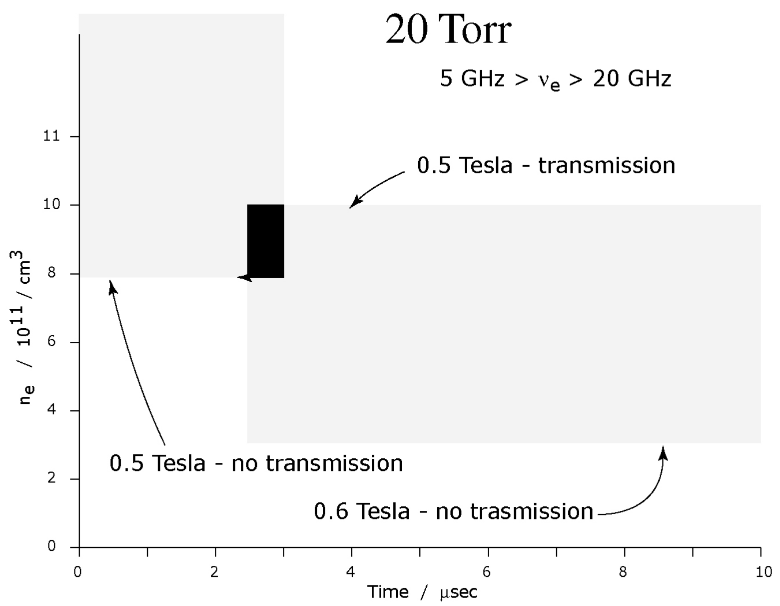

Fig 4.14: Electron number density for 20 Torr plasma over one 10 µsec pulser cycle.

With this parametric study it was possible to determine unambiguously the plasma collisional frequency. By means of this value, it was possible to time resolving the measurement of the electron number density, as it is possible to see in figures 4.15, 4.16, 4.17.

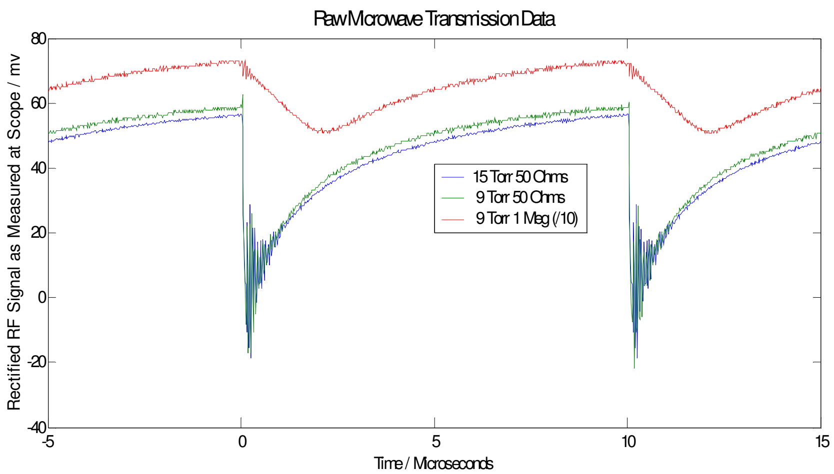

Fig 4.15: Measured time resolved attenuation of the 12.6 GHz microwave source.

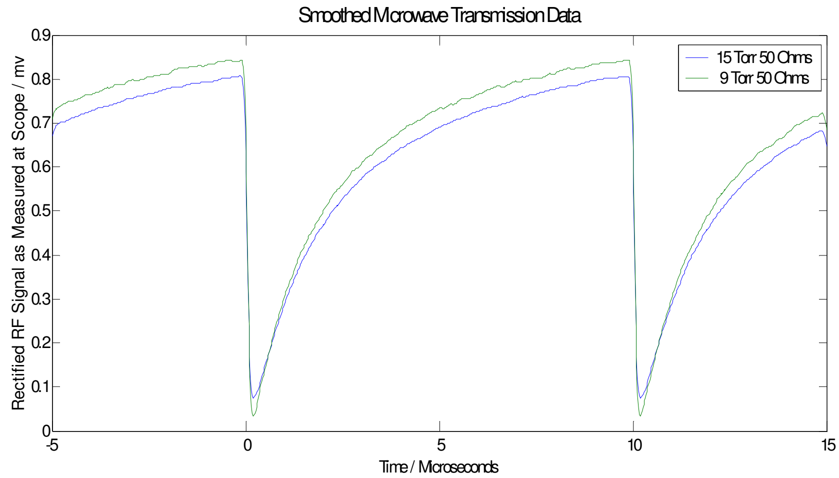

Fig 4.16: Smoothed time resolved attenuation of the 12.6 GHz microwave source.

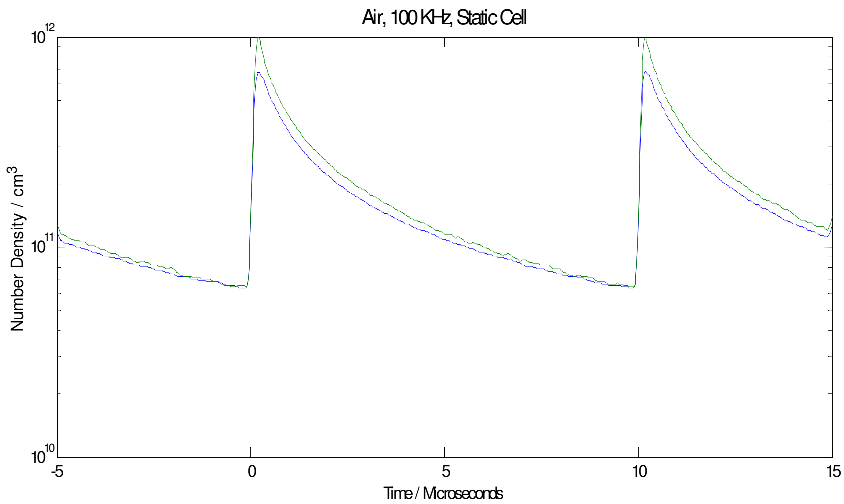

Fig 4.17: Time resolved electron number density, same key as in fig 4.16.

Conclusions

A volume filling, uniform, non-equilibrium, cold plasma has been produced in a Mach 3 air flow using 2 ns, 100 kHz repetition rate, 30 kV pulses. Theoretical analysis indicates the electron number density to be on the order of 5×10^{11}-10^{12} cm^{-3}.

The 5 Tesla magnetic field was shown to improve the uniformity of the plasma and had a dramatic effect in confining the plasma to the inter-electrode volume.

An experimental observation of an MHD electric field in MHD generator with non-equilibrium ionization in cold supersonic flows has been made.

By varying an applied bias voltage across the MHD channel, the Faraday voltage was measured to be 60% of the theoretical value.

Electron number densities and collision frequencies were evaluated by varying the intensity of the applied magnetic field and observing conditions corresponding to complete absorption/reflection of the diagnostic microwaves. The number densities generated by the pulsed ionization scheme were found to peak at about 10^{12} per cm^3. Over the 10 msec decay time between pulses the number densities were observed to decay to about 2 $x10^{11}$ per cm^3 using 1 Torr of air in the cell and $5x10^{11}$ per cm^3 using 20 Torr of air in the static cell.

References

[i] Macheret S.O., Shneider M.N., and Miles R.B., "Modeling of Air Plasma Generation by Electron Beams and High-Voltage Pulses," AIAA Paper 2000-2569, June 2000.
[ii] Bychkov Yu I., Korolev Yu. D., and Mesyats G.A., *Injection Gaseous Electronics*, Nauka, Moscow, 1982.
[iii] Berger M.J. and Seltzer S.M., *Tables of Energy Losses and Ranges of Electrons and Positrons*, NASA SP-3012, 1964.
[iv] Grundy R.F., Magnetohydrodynamic Energy for Electric Power Generation, Noyes Data Corporation, New Jersey, 1978.
[v] R.R. Holman and T.E. Lippert, *Energy Conversion Alternatives Study, Westinghouse Phase I Final Report*, Volume X, *Liquid Metal MHD Systems*, Westinghouse Electric Corporation Research Laboratories, Report N76-23701, February 1976.
[vi] Mullaney G. and Dibelius N.R., "Electrical Conductivity of Flames seeded with Large Concentrations of Sodium, Barium and Strontium," in *"Advances in Magnetohydrodynamics"*, Edited by McGrath I.A., Siddall R.G., and Thring M.W., Proceedings of a Colloquium, Department of Fuel Technology and Chemical Engineering, Sheffield University, Oct. 1961, Pergamon Press LTD., 1963.
[vii] Muntenbruch H., "Technical Problems," in *MHD Power Generation: Selected Problems of Combustion MHD Generators*, edited by J. Raeder, Springer-Verlag, New York, 1975.
[viii] Curran, E.T. and S.N.B. Murthy, ed. 2000. *Scramjet Propulsion*. AIAA Progress in Astronautics and Aeronautics, v 189.
[ix] Raizer Yu. P., *Gas Discharge Physics*, Springer, Berlin, 1991.
[x] Macheret S.O., Shneider M.N., and Miles R.B., "Modeling of air plasma generation by repetitive high-voltage nanosecond pulses," IEEE Transactions on Plasma Science, Vol. 30, 2002, pp. 1301-1314
[xi] Macheret S.O., Shneider M.N., and Miles R.B., "Modelling for Discharges generated by Electron Beams in Dense Gases: Fountain and Thunderstorm Regimes," *Physics of Plasmas*, Vol. 8, No. 5, 2001, pp. 1518-1528
[xii] Macheret S.O., Shneider M.N., and Miles R.B., "Magnetohydrodynamic Control of Hypersonic Flows and Scramjet Inlets Using Electron Beam Ionization," *AIAA Journal*, Vol. 36, No. 1, Jan. 2002, pp. 74-81.
[xiii] Mother.chtm.unm.edu/mojahed/homepage
[xiv] Huddlestone, R.H. and S.L. Leonard, ed. *Plasma Diagnostics Techniques*. New York, 1965.
[xv] Kurpik, A., Menart, J., Shang, J., Kimmel, R., Hayes, J., "Technique for Making Microwave Absorption Measurements in a Small Plasma Discharge," AIAA Paper 2003-3748, 34th AIAA Plasmadynamics and Lasers Conference, Orlando, Jan. 22-26, 2003.
[xvi] Murray R.M., Zaidi S.H., Shneider M.N., Macheret S.O., Miles R.B., Kline J.F., Nonequilibrium Ionization Techniques For MHD Power Extraction in

High-Speed Flows, 41st Aerospace Sciences Meeting and Exhibit, AIAA-2003-1049, 6-9 January Reno, 2003.